Competing orders at higher-order Van Hove points

Laura Classen,[1,2] Andrey V. Chubukov,[1] Carsten Honerkamp,[3,4] and Michael M. Scherer[5]
[1]*School of Physics and Astronomy, University of Minnesota, Minneapolis, Minnesota 55455, USA*
[2]*Condensed Matter Physics and Materials Science Department, Brookhaven National Laboratory, Upton, New York 11973, USA*
[3]*Institute for Theoretical Solid State Physics, RWTH Aachen University, 52074 Aachen, Germany*
[4]*JARA-FIT, Jülich Aachen Research Alliance and Fundamentals of Future Information Technology, 52056 Aachen, Germany*
[5]*Institut für Theoretische Physik, Universität zu Köln, 50937 Cologne, Germany*

(Received 2 July 2020; revised 7 September 2020; accepted 9 September 2020; published 24 September 2020)

Van Hove points are special points in the energy dispersion, where the density of states exhibits analytic singularities. When a Van Hove point is close to the Fermi level, tendencies towards density wave orders, Pomeranchuk orders, and superconductivity can all be enhanced, often in more than one channel, leading to a competition between different orders and unconventional ground states. Here we consider the effects from higher-order Van Hove points, around which the dispersion is flatter than near a conventional Van Hove point, and the density of states has a power-law divergence. We argue that such points are present in intercalated graphene and other materials. We use an effective low-energy model for electrons near higher-order Van Hove points and analyze the competition between different ordering tendencies using an unbiased renormalization-group approach. For purely repulsive interactions, we find that two key competitors are ferromagnetism and chiral superconductivity. For a small attractive interaction, we find an unconventional spin Pomeranchuk order, in wich the spin oder parameter winds around the Fermi surface. The supermetal state, predicted for a single higher-order Van Hove point, is an unstable fixed point in our case.

DOI: 10.1103/PhysRevB.102.125141

I. INTRODUCTION

The competition between different types of ordering tendencies plays a key role in many quantum materials. For example, unconventional superconductivity often develops near a charge or spin order and is viewed as mediated by soft charge or spin fluctuations. Within an itinerant electron scenario, the formation of an ordered phase can be understood as an instability of the parent electron liquid, driven by excitations around the Fermi energy. Therefore, the density of states (DOS) near the Fermi level and the geometry of the Fermi surface strongly affect the low-energy phase formation. In a two-dimensional crystal, both quantities can change significantly when the fermionic dispersion possesses a saddle point, which is one of the prominent examples of Van Hove points [1]. The DOS near such a point diverges logarithmically and the Fermi surface transforms between a holelike and electronlike form. If the Fermi level lies in the vicinity of a Van Hove point, the singular DOS determines the physical behavior due to the large number of available low-energy states. In particular, interaction effects get amplified not only in the particle-particle, but also in the particle-hole channels, leading to the notion of competing orders. A prototypical example is the interplay of spin-density-wave order and d-wave superconductivity near Van Hove filling in the Hubbard model on the square lattice [2].

For electrons on the honeycomb lattice, e.g., in single-layer graphene, the competition is again between d-wave superconductivity and spin-density-wave order, but the ordered states are more nontrivial: d-wave superconductivity is chiral [3–7], and spin-density-wave order is a half metal [8], which additionally breaks lattice translational symmetry [9]. On the other hand, while for square-lattice systems the Van Hove points are located reasonably close to the Fermi level already at charge neutrality, they are at higher energies for electrons on the honeycomb lattice, and it requires a substantial amount of doping to reach them. Recently, such doping levels have been made accessible by intercalation of graphene [10,11]. The intercalation leads to a renormalization of the band structure, which reduces the bandwidth and, hence, the value of the chemical potential required to bring the Van Hove points to the Fermi level. However, the intercalation also brings another effect: it flattens the band dispersion around the Van Hove points. This flattening gives rise to a stronger power-law singularity of the DOS, which can qualitatively affect the balance between different ordering tendencies. In particular, it suppresses finite wave-vector density-wave fluctuations and enhances fluctuations with zero-momentum transfer, e.g., Stoner-type instabilities. Consequently, a new type of competition occurs between the pairing and zero-momentum instabilities in the particle-hole channel.

A Van Hove point with a power-law divergence of the DOS has been termed a higher-order Van Hove (HOVH) point, as opposed to a conventional Van Hove (CVH) point. HOVH points were proposed to exist in moiré superlattices, e.g., twisted bilayer graphene and trilayer graphene, in which the twist angle, pressure, or an electric field can be used to tune the band structure [12]. Germanene on MoS_2 shows similar

effects as intercalated graphene: a reduced Van Hove energy and the band flattening around the Van Hove points [13]. Other examples for systems with HOVH points include biased bilayer graphene at charge neutrality [14] and magnetic-field-tuned $Sr_3Ru_2O_7$ [15] and β-$YbAlB_4$ [16]. The case of a single HOVH point in the Brillouin zone has recently been studied in Ref. [17]. It was shown that fluctuations around this single HOVH point drive the system towards a critical non-Fermi-liquid ground state, dubbed a supermetal.

In this paper, we analyze the competition of ordering tendencies arising from the presence of *multiple* HOVH points near the Fermi level. In this more general case, additional types of couplings occur, and we show that the supermetal state becomes an unstable fixed point. Instead, the system develops an instability towards either superconductivity or Pomeranchuk order.

We set up a renormalization-group (RG) framework within an effective low-energy model for electrons near the HOVH points, with parameters appropriate for gadolinium-doped graphene. This allows us to account for the interplay between different ordering tendencies and identify the leading instability. We show that chiral superconductivity can still develop, as for the case of a CVH point, but the pair-hopping term, which drives it, needs to be sufficiently strong compared to other couplings. For other ranges of interactions, we find a ferromagnetic instability and a special d-wave spin Pomeranchuk order, in which the spin order parameter winds around the Fermi surface.

II. HIGHER-ORDER VAN HOVE SINGULARITY IN GRAPHENE

It was shown in Ref. [10] that the doping levels needed to reach the Van Hove energy in graphene can be made accessible by intercalation, with large-scale homogeneity and very good crystallinity. In the process, the electronic spectrum undergoes strong renormalizations, which not only bring down the Van Hove energy but also flatten the energy dispersion around the M points, i.e., transform CVH points into HOVH points. While electronic correlations may be responsible for the band renormalization [10], we can model their effect by introducing an effective single-particle Hamiltonian for electrons on the honeycomb lattice with hopping up to the third neighbor. This allows us to qualitatively reproduce the observed band flattening along the K-M direction and the measured Fermi-surface geometry. However, we emphasize that our analysis of the competing orders below does not depend on the precise band structure or the mechanisms causing it.

A. Effective hopping Hamiltonian

The effective Hamiltonian including up to third-neighbor hopping reads

$$H_0 = \Big[t_1 \sum_{\langle i,j\rangle,\sigma} c^\dagger_{i\sigma} c_{j\sigma} + t_2 \sum_{\langle\langle i,j\rangle\rangle,\sigma} c^\dagger_{i\sigma} c_{j\sigma} + t_3 \sum_{\langle\langle\langle i,j\rangle\rangle\rangle,\sigma} c^\dagger_{i\sigma} c_{j\sigma} + \text{H.c.} \Big] - \mu \sum_{i\sigma} n_{i\sigma}. \quad (1)$$

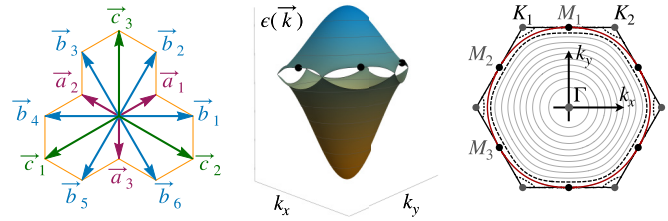

FIG. 1. Lattice and tight-binding model. Left panel: Lattice in real space with neighboring vectors $\vec{a}_n, \vec{b}_n, \vec{c}_n$. The nearest-neighbor vectors on the honeycomb lattice are $\vec{a}_1 = (\sqrt{3}, 1)/2$, $\vec{a}_2 = (-\sqrt{3}, 1)/2$, $\vec{a}_3 = (0, -1)$; the second-nearest-neighbor vectors are $\vec{b}_1 = (\sqrt{3}, 0), \vec{b}_2 = (\sqrt{3}, 3)/2, \vec{b}_3 = (-\sqrt{3}, 3)/2$, $\vec{b}_4 = -\vec{b}_1, \vec{b}_5 = -\vec{b}_2, \vec{b}_6 = -\vec{b}_3$; and the third-nearest-neighbor vectors are $\vec{c}_1 = -2\vec{a}_1, \vec{c}_2 = -2\vec{a}_2, \vec{c}_3 = -2\vec{a}_3$. Middle panel: Energy dispersion for $t_1 = 1, t_2 = 0.1, t_3 = 0.2$. The valence and conduction band touch at the Dirac points. The Van Hove points appear at the M points, which are marked by black dots for the conduction band. Right panel: Energy contours for the same hopping amplitudes and the high-symmetry points $K_1 = 2\pi/3(1/\sqrt{3}, 1)$, $K_2 = 2\pi/3(-1/\sqrt{3}, 1)$ and $M_1 = \pi(0, 2/3)$, $M_2 = \pi(-1/\sqrt{3}, 1/3)$, $M_3 = -\pi(1/\sqrt{3}, 1/3)$. The Fermi level at Van Hove filling is given by the red line. At this filling, the system undergoes a Lifshitz transition from a closed to an open Fermi surface. For a small variation of the filling, the Fermi surface is either closed as demonstrated by the nearby dashed line, or changes to open Fermi-surface pockets given by the dotted lines around the K points.

We have introduced $c^{(\dagger)}_{i,\sigma}$ as the fermion annihilation (creation) operator at site i and spin projection $\sigma \in \{\uparrow, \downarrow\}$. The nearest-, second-nearest-, and third-nearest-neighbor hopping amplitudes are t_1, t_2, and t_3, and the Fermi level can be adjusted with the chemical potential μ. We have defined $n_{i,\sigma} = c^\dagger_{i\sigma} c_{i\sigma}$ as the particle number operator. The honeycomb lattice and the locations of first, second, and third neighbors are sketched in Fig. 1.

From the model Eq. (1) we obtain the energy bands

$$\epsilon_\pm(\vec{k}) = \pm|t_1\alpha(\vec{k}) + t_3\gamma(\vec{k})| - t_2\beta(\vec{k}) - \mu, \quad (2)$$

with $\alpha(\vec{k}) = \sum_{n=1}^3 e^{-i\vec{k}\cdot\vec{a}_n}$, $\beta(\vec{k}) = \sum_{n=1}^6 e^{-i\vec{k}\cdot\vec{b}_n}$, and $\gamma(\vec{k}) = \sum_{n=1}^3 e^{-i\vec{k}\cdot\vec{c}_n}$, where $\vec{a}_n, \vec{b}_n, \vec{c}_n$ denote nearest-, second-nearest-, and third-nearest-neighbor vectors (see Fig. 1).

The energy dispersion and the corresponding Fermi surface depend on the choice of the hopping amplitudes t_1, t_2, t_3 and the chemical potential μ. For definiteness, we consider the branch $\epsilon_+(\vec{k})$ and discuss how it changes with the chemical potential. At small μ, the Fermi surface consists of six pockets around the Dirac points (see Fig. 1). As μ increases, the edges of the Fermi pockets come closer to each other, and at

$$\mu = t_1 + 2t_2 - 3t_3 \quad (3)$$

they merge at the three special high-symmetry points on the edges of the first Brillouin zone, i.e., M_1, M_2, M_3 (see Fig. 1). At larger μ, the Fermi surface is a closed loop, centered at the Γ point.

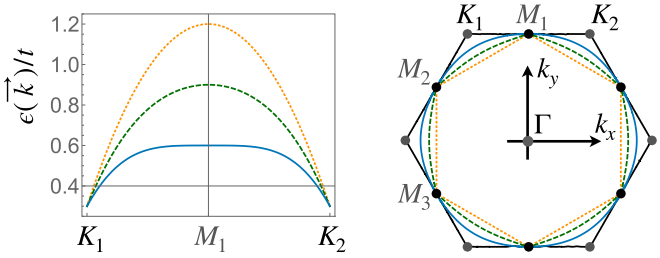

FIG. 2. Band flattening at Van Hove point. Left panel: Dispersion along $K_1 - M_1 - K_2$ for fixed $t_2 = 0.1t_1$ and varying $t_3 = 0$ (orange, dotted), $t_3 = 0.1t_1$ (green, dashed), and $t_3 = 0.2t_2$ (blue, solid). The last value of t_3 leads to a HOVH singularity. Right panel: Corresponding Fermi surface.

The points M_p, $p \in \{1, 2, 3\}$, are Van Hove points. We can verify this by expanding the dispersion around them:

$$\epsilon_{M_1}(\vec{x}) = b_1 y^2 - a_1 x^2 + \cdots , \tag{4}$$

$$\epsilon_{M_2}(\vec{x}) = a_2 x^2 - c_2 xy + b_2 y^2 + \cdots = b_2[y - c_2 x/(2b_2)]^2 - \frac{1}{b_2}\left(c_2^2/4 - a_2 b_2\right)x^2 + \cdots , \tag{5}$$

$$\epsilon_{M_3}(\vec{x}) = a_2 x^2 - c_2 xy + b_2 y^2 + \cdots = b_2[y + c_2 x/(2b_2)]^2 - \frac{1}{b_2}\left(c_2^2/4 - a_2 b_2\right)x^2 + \cdots , \tag{6}$$

where $\epsilon_{M_p}(x, y) = \epsilon_{\pm}(M_{p,x} + x, M_{p,y} + y) + \mu$, and the dots denote higher-order terms in x, y. The coefficients are given by the hoppings t_1, t_2, t_3 (see Appendix A). All $a_p, b_p, c_p \geqslant 0$ and $c_p \geqslant (2a_2 b_2)^{1/2}$. Since the dispersion is quadratic, with opposite signs along the two directions, the DOS is logarithmically singular. This holds as long as the prefactors are nonzero, i.e., $a_1, b_1 > 0$ for $\epsilon_{M_1}(\vec{x})$ and $b_2, (c_2^2/4 - a_2 b_2) > 0$ for $\epsilon_{M_{2/3}}(\vec{x})$.

B. Higher-order Van Hove points

The CVH points become HOVH points when one of the prefactors in Eq. (4) vanishes, and one has to expand further to get the dispersion in the corresponding direction. In our model this happens for

$$t_3 \to t_{3,c} = (t_1 - 2t_2)/4. \tag{7}$$

For this special case, a_1 and $c_2^2/4 - a_2 b_2$ in Eq. (4) vanish. We show the flattening of the dispersion for increasing t_3 in Fig. 2, together with the change of the Fermi surface, which becomes rounder. This qualitatively mimics the effect observed for gadolinium intercalation in graphene [10].

For $t_3 = t_{3,c}$, we have to expand to higher order, i.e.,

$$\epsilon_{M_1}(\vec{x}) = b_1 y^2 - d_1 x^4 + \cdots , \tag{8}$$

$$\epsilon_{M_2}(\vec{x}) = b_2[y - c_2 x/(2b_2)]^2 - d_2 x^4 + \cdots , \tag{9}$$

$$\epsilon_{M_3}(\vec{x}) = b_2[y + c_2 x/(2b_2)]^2 - d_2 x^4 + \cdots , \tag{10}$$

with $d_{1,2} > 0$. The saddle-type dispersion near this HOVH point is shown in Fig. 3. For such a dispersion, the DOS shows

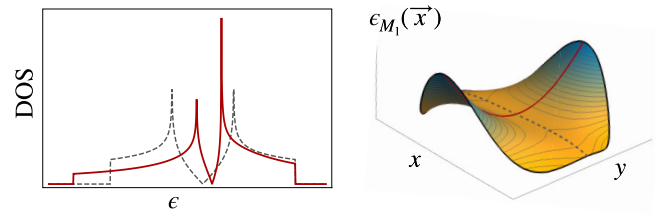

FIG. 3. DOS and saddle point. Left panel: DOS of the band dispersion for hopping parameters $t_1 = 1, t_2 = 1/10, t_3 = \frac{1}{4}(1 - 2/10)$ (solid line) and DOS for hopping parameters $t_1 = 1, t_2 = t_3 = 0$ for comparison (dashed line). Right panel: Corresponding higher-order saddle point at M_1.

a power-law divergence:

$$\rho(\epsilon) = \begin{cases} \rho_+ \epsilon^{-1/4} & \text{for } \epsilon > 0, \\ \rho_- |\epsilon|^{-1/4} & \text{for } \epsilon < 0, \end{cases} \tag{11}$$

where $\rho_+ = \Gamma[1/4]/[8\pi^{5/2}(b_1^2 d_1)^{1/4}]$ and $\rho_- = \rho_+/\sqrt{2}$ (see Ref. [17]). This divergence is stronger than the logarithmic one at a CVH point. The singular behavior of the DOS near the HOVH point can be determined from a scaling argument [18] (see Appendix A); for an alternative see Ref. [19].

We also consider the generalized case with

$$\epsilon_{M_1}(\vec{x}) = b_1 y^2 - d_1 x^{2\alpha} + \cdots , \tag{12}$$

$$\epsilon_{M_2}(\vec{x}) = b_2[y - c_2 x/(2b_2)]^2 - d_2 x^{2\alpha} + \cdots , \tag{13}$$

$$\epsilon_{M_3}(\vec{x}) = b_2[y + c_2 x/(2b_2)]^2 - d_2 x^{2\alpha} + \cdots , \tag{14}$$

where $\alpha > 1$. The case $\alpha = 1$ corresponds to a CVH point; the case $\alpha = 2$ corresponds to the HOVH point in our model of intercalated graphene. For $\alpha < 2$, this generalized saddle-point dispersion can also be interpreted to effectively model the case where the system is slightly doped away from a HOVH point.

The DOS for the generalized dispersion in Eq. (12) is

$$\rho(\epsilon) = \begin{cases} \rho_+ \epsilon^{-\kappa} & \text{for } \epsilon > 0, \\ \rho_- |\epsilon|^{-\kappa} & \text{for } \epsilon < 0, \end{cases} \tag{15}$$

where $\kappa = 1/2 - 1/(2\alpha)$, $\rho_+ = \Gamma[1/(2\alpha)]\Gamma[1/2 - 1/(2\alpha)]/(4\alpha\pi^{5/2} b_1^{1/2} d_1^{1/(2\alpha)})$, and $\rho_- = \rho_+ \sin[\pi/(2\alpha)]$ (see Ref. [17]). For $\alpha = 2$, we recover $\kappa = 1/4$. When $\alpha \to 1$, $\kappa \to 0$, and $\rho_\pm$ formally diverges as $1/\kappa$. The divergence becomes $[1 - (\epsilon/\Lambda)^\kappa]/\kappa = \ln \Lambda/\epsilon$, once we keep a UV cutoff Λ. The logarithmic divergence is the expected result for a CVH point. There are other examples of systems with a HOVH singularity with various exponents. The HOVH singularity in twisted bilayer graphene is also described by $\kappa = 1/4$ (see Ref. [12]). In bilayer graphene, one can tune the dispersion with an interlayer voltage bias to a power-law singularity with $\kappa = 1/3$ at charge neutrality [14]. $Sr_3Ru_2O_7$ [15] and β-$YbAlB_4$ [16] are expected to have a HOVH singularity with $\kappa = 1/2$.

III. PATCH MODEL

Because the DOS has a power-law singularity near the HOVH points, the low-energy physics is determined by fermions with momenta near these points. Accordingly, we restrict our consideration to momentum states in patches around

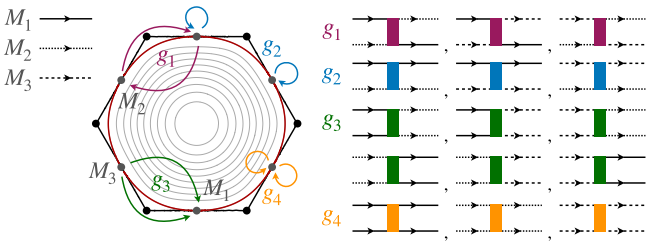

FIG. 4. Three-patch model and interaction couplings. Graphic representation of the four interaction couplings g_i, $i \in \{1, \ldots, 4\}$ representing the scattering processes between the three M_p points for the Van Hove doped dispersion. Solid, dashed, and dotted lines represent electrons near the three M_p points.

the HOVH points. The patch size is related to the UV energy cutoff Λ. We assume that degrees of freedom with energies larger than Λ are integrated out, and microscopic information is incorporated into the bare parameters of the effective patch model.

Within the effective model, we include all scattering processes between fermions near the HOVH points, allowed by symmetry and momentum conservation. This gives four different couplings g_i, $i \in \{1, \ldots, 4\}$, like for the case of CVH points at M_p (see Ref. [3]). The interaction part of the effective Hamiltonian then reads

$$H_g = \sum_{\substack{k_1 \ldots k_3 \\ \sigma\sigma'}} \sum_{\substack{p,\, p' = 1 \\ p \neq p'}}^{3} \big[g_1 c^\dagger_{p'\sigma k_3} c^\dagger_{p\sigma k_4} c_{p'\sigma' k_2} c_{p\sigma k_1} + g_2 c^\dagger_{p\sigma k_3} c^\dagger_{p'\sigma k_4} c_{p'\sigma' k_2} c_{p\sigma k_1} + g_3 c^\dagger_{p'\sigma k_3} c^\dagger_{p'\sigma k_4} c_{p\sigma' k_2} c_{p\sigma k_1} \big] + \sum_{\substack{k_1 \ldots k_3 \\ \sigma\sigma'}} \sum_{p=1}^{3} g_4 c^\dagger_{p\sigma k_3} c^\dagger_{p\sigma k_4} c_{p\sigma' k_2} c_{p\sigma k_1}. \tag{16}$$

Here, $c_{p\sigma k}$ is the annihilation operator for an electron in the vicinity of the point M_p, $p \in \{1, 2, 3\}$, with momentum $M_p + k$ and spin σ. The momentum k is restricted to the patch around M_p. The couplings are independent on the flavor index p due to sixfold rotational symmetry. The scattering processes are sketched in Fig. 4. We note in passing that an analogous description can be derived for the square lattice with the only difference that there are only two patches $p = 1, 2$ (see Ref. [20]).

IV. SUSCEPTIBILITIES

The interactions receive corrections through different scattering channels. These corrections grow with decreasing T and, if the dressed interaction diverges at a finite T in at least one channel, the Fermi liquid is not the stable ground state. In the patch model, potential divergences can occur in the particle-particle or particle-hole channel, due to processes with momentum transfer near zero or near M_p. To understand the relative strength of various corrections, we first compute the corresponding particle-particle and particle-hole susceptibilities for free fermions, i.e.,

$$\chi^X_{\rm pp} := T \sum_\omega \int \frac{d^2k}{(2\pi)^2} G_0(\omega, k) G_0(-\omega, X - k), \tag{17}$$

$$\chi^X_{\rm ph} := -T \sum_\omega \int \frac{d^2k}{(2\pi)^2} G_0(\omega, k) G_0(\omega, X + k), \tag{18}$$

where $G_0(\omega, q) = 1/[i\omega - \epsilon(q)]$ and the wave vector X is either zero or M_p. We have set the frequency transfer to zero because there the corrections are the largest.

For $\kappa = 0$, i.e., the case of a CVH singularity, $\chi^0_{\rm pp}$ diverges as $\ln^2 \Lambda/T$, and $\chi^{M_p}_{\rm ph}$ diverges either as $\ln^2 \Lambda/T$ for a nested Fermi surface with nesting vector M_p or as $\ln \Lambda/T$ for nonperfect nesting [3,20]. The susceptibilities $\chi^{M_p}_{\rm pp}$ and $\chi^0_{\rm ph}$ diverge less strongly, as $\ln \Lambda/T$ even for perfect nesting. Then the thermal evolution of the couplings comes primarily from renormalizations in the particle-particle channel at zero-momentum transfer and in the particle-hole channel at momentum transfer M_p, leading to a competition between tendencies towards a spin-density-wave order and superconductivity. The situation changes qualitatively at a HOVH point, where the DOS diverges with a power law. We will show below that in this case $\chi^0_{\rm pp}$ and $\chi^0_{\rm ph}$ diverge as $1/T^\kappa$, while $\chi^{M_p}_{\rm pp}$ remains logarithmically singular, and $\chi^{M_p}_{\rm ph}$ becomes constant. In this case, the key ordering tendencies are superconductivity and $q = 0$ spin and charge orders.

A. Zero-momentum transfer

The particle-hole susceptibility with zero-momentum transfer is

$$\begin{aligned}\chi^0_{\rm ph} &= -T \sum_\omega \int \frac{d^2k}{(2\pi)^2} \frac{1}{[i\omega - \epsilon_M(k)]^2} \\ &= -T \sum_\omega \int d\epsilon \rho(\epsilon) \frac{\partial}{\partial \epsilon} \frac{1}{i\omega - \epsilon} = -\int d\epsilon \rho(\epsilon) \frac{\partial}{\partial \epsilon} n_F(\epsilon) \\ &= \frac{1}{4T} \int d\epsilon \frac{\rho_0}{|\epsilon|^\kappa} \frac{1}{\cosh^2(\epsilon/2T)} \\ &= \frac{\rho_0}{T^\kappa} f(\kappa),\end{aligned} \tag{19}$$

where $n_F(\epsilon)$ is the Fermi function, $\rho_0 = (\rho_+ + \rho_-)/2$, and we defined $f(\kappa) = \frac{1}{4} \int d\epsilon\, |\epsilon|^{-\kappa} \cosh^{-2}(\epsilon/2)$. In the limit $\kappa \to 1/4$, we obtain $f(\kappa = 1/4) \approx 1.08$. For $\kappa \to 0$, the DOS becomes a logarithmic function and we recover the logarithmic temperature dependence in $\chi^0_{\rm ph}$. We see that, for $\kappa > 0$, $\chi^0_{\rm ph}$ increases by a power law as T decreases.

For the particle-particle susceptibility $\chi^0_{\rm pp}$, using inversion symmetry $\epsilon(k) = \epsilon(-k)$, we obtain

$$\begin{aligned}\chi^0_{\rm pp} &= T \sum_\omega \int \frac{d^2k}{(2\pi)^2} \frac{1}{[i\omega - \epsilon_M(k)][-i\omega - \epsilon_M(-k)]} \\ &= -\int d\epsilon \rho(\epsilon) \frac{n_F(\epsilon) - n_F(-\epsilon)}{2\epsilon} \\ &= \frac{\rho_0}{T^\kappa} g(\kappa),\end{aligned} \tag{20}$$

where $g(\kappa) = \frac{1}{2}\int d\epsilon\, |\epsilon|^{-(1+\kappa)} |\tanh(\epsilon/2)|$. For $\kappa = 1/4$, $g(1/4) \approx 4.33$, for $\kappa \to 0$, $g(\kappa \to 0) \propto 1/\kappa$. Combining the last behavior with the logarithmic divergence of the DOS in this limit, we find $\chi^0_{\rm pp} \propto (\ln \Lambda/T)^2$, as expected for a CVH point.

B. Finite momentum transfer

In contrast to $\chi^0_{\rm pp/ph}$, the susceptibilities at the momentum transfer M_p do not exhibit a power-law divergence. For definiteness, we consider $\chi^{M_1}_{\rm pp/ph}$. For the particle-hole susceptibility we obtain

$$\begin{aligned}\chi^{M_1}_{\rm ph} &= -T\sum_{\omega}\int \frac{d^2k}{(2\pi)^2}\frac{1}{\left[i\omega-\epsilon_{M_3}(k)\right]\left[(i\omega-\epsilon_{M_2}(k)\right]}\\ &= -\int \frac{d^2k}{(2\pi)^2}\frac{n_F\left[\epsilon_{M_3}(k)\right]-n_F\left[\epsilon_{M_2}(k)\right]}{\epsilon_{M_3}(k)-\epsilon_{M_2}(k)}\\ &\approx \frac{1}{2\tilde{c}_2}\int^{\frac{\Lambda}{T}}\frac{d^2\tilde{k}}{(2\pi)^2}\frac{\frac{1}{\tilde{k}_x\tilde{k}_y}\sinh(\tilde{c}_2\tilde{k}_x\tilde{k}_y)}{\cosh\left(\tilde{k}_x^2+\tilde{k}_y^2\right)+\cosh(\tilde{c}_2\tilde{k}_x\tilde{k}_y)},\end{aligned} \tag{21}$$

where we have rescaled $k_x = \sqrt{T/a_2}\tilde{k}_i$, $k_y = \sqrt{T/b_2}\tilde{k}_y$ and introduced $\tilde{c}_2 = c_2/\sqrt{a_2 b_2}$. For the case of a pure HOVH point, $\tilde{c}_2 = 2$. In this case, $\chi^{M_1}_{\rm ph}$ remains finite. Indeed, a potential singular temperature dependence in Eq. (21) can come from the singularity at the upper limit of the integration over $d^2\tilde{k}$ for $\Lambda/T \to \infty$. Using polar coordinates, we can reexpress the potential singularity in Eq. (21) as

$$\int^{\frac{\Lambda}{T}}\frac{dr}{r}\int_{\sin(2\phi)>2/\tilde{c}}\frac{d\phi}{\sin(2\phi)}\frac{e^{r^2[\frac{\tilde{c}}{2}\sin(2\phi)-1]}}{1+e^{r^2[\frac{\tilde{c}}{2}\sin(2\phi)-1]}}. \tag{22}$$

In case $\tilde{c}_2 = 2$, the integration over ϕ gives $1/r^2$, and the integral over r converges, i.e.,

$$\chi^{M_1}_{\rm ph} \to \text{const.} \tag{23}$$

For a quadratic dispersion along the x direction $\tilde{c}_2 > 2$. In this case, there is a finite range of angles ϕ, for which $(\tilde{c}/2)\sin\phi > 1$. In this range, the integration over ϕ now yields a finite number, and the integral over r gives $\ln \Lambda/T$. This is the expected behavior for a CVH point.

For $\chi^M_{\rm pp}$, we obtain

$$\begin{aligned}\chi^{M_1}_{\rm pp} &= -T\sum_{\omega}\int \frac{d^2k}{(2\pi)^2}\frac{1}{\left[i\omega-\epsilon_{M_3}(k)\right]\left[i\omega+\epsilon_{M_2}(k)\right]}\\ &= -\int \frac{d^2k}{(2\pi)^2}\frac{n_F\left[\epsilon_{M_3}(k)\right]-n_F\left[-\epsilon_{M_2}(k)\right]}{\epsilon_{M_3}(k)+\epsilon_{M_2}(k)}\\ &\approx \frac{1}{2}\int^{\frac{\Lambda}{T}}\frac{d^2\tilde{k}}{(2\pi)^2}\frac{\frac{\sqrt{a_2 b_2}}{\tilde{k}_x^2+\tilde{k}_y^2}\sinh(\tilde{k}_x^2+\tilde{k}_y^2)}{\cosh\left(\tilde{k}_x^2+\tilde{k}_y^2\right)+\cosh(\tilde{c}_2\tilde{k}_x\tilde{k}_y)}.\end{aligned} \tag{24}$$

Using polar coordinates, we find that

$$\chi^{M_1}_{\rm pp} \propto \ln\frac{\Lambda}{T}. \tag{25}$$

This result holds for all κ. To verify the expressions for the susceptibilities, we computed $\chi^0_{\rm ph/pp}$ and $\chi^M_{\rm ph/pp}$ numerically, by integrating over the entire Brillouin zone (see Appendix B). We obtained the same behavior as in the patch model.

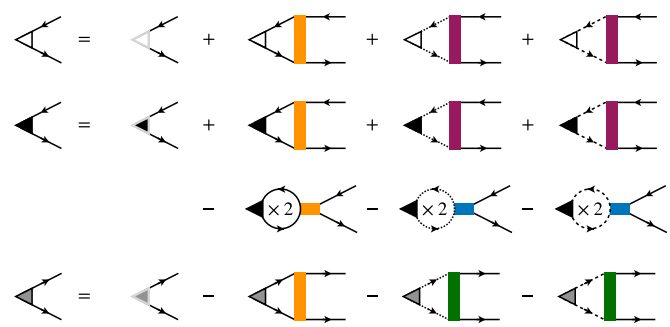

FIG. 5. Ladder series for vertices. Graphic representation of the ladder series for the spin (top row), charge (middle rows), and pairing (bottom row) vertex. States close to the three M_p points are represented by solid, dashed, and dotted lines. The couplings are colored according to Fig. 4.

C. Ladder series

The divergences that we found in $\chi^0_{\rm pp}$ and $\chi^0_{\rm ph}$ can lead to a pairing or to a $q = 0$ instability in either spin or charge channel, when we separately sum up the corresponding ladder series. We follow a standard protocol and introduce three types of infinitesimally small trial (bare) vertices $\Gamma^0_{\rm SC}$, Γ^0_s, and Γ^0_c, where SC stands for superconducting, and $s(c)$ stands for spin (charge). Because there are three nonequivalent HOVH points, each vertex is a three-component vector: $\hat{\Gamma}^0_i = (\Gamma^0_i(M_1), \Gamma^0_i(M_2), \Gamma^0_i(M_3))$ $(i = {\rm SC}, c, s)$.

The full vertices $\hat{\Gamma}_i$ are obtained by summing up ladder series of renormalizations. In each section of a ladder we have the product of some combination of the couplings g_i and either $\chi^0_{\rm pp}$ or $\chi^0_{\rm ph}$. The ladder series are shown graphically in Fig. 5. In analytical form, we obtain

$$\begin{aligned}\hat{\Gamma}_s &= \hat{\Gamma}^0_s + \hat{\Gamma}_s\hat{A}_s\chi^0_{\rm ph},\\ \hat{\Gamma}_c &= \hat{\Gamma}^0_c + \hat{\Gamma}_c\hat{A}_c\chi^0_{\rm ph},\\ \hat{\Gamma}_{\rm SC} &= \hat{\Gamma}^0_{\rm SC} + \hat{\Gamma}_{\rm SC}\hat{A}_{\rm SC}\chi^0_{\rm pp},\end{aligned} \tag{26}$$

where $\hat{A}_i$ are 3×3 matrices:

$$\hat{A}_i = \begin{pmatrix} d_i & o_i & o_i\\ o_i & d_i & o_i\\ o_i & o_i & d_i\end{pmatrix} \tag{27}$$

with the matrix elements being combinations of the couplings, i.e., $d_s = g_4$, $o_s = g_1$, $d_c = -g_4$, $o_c = g_1 - 2g_2$, $d_{\rm SC} = -g_4$, $o_{\rm SC} = -g_3$. We have absorbed a constant into Γ^0_i. Each matrix equation can be decomposed into three independent equations for the eigenvectors:

$$\begin{aligned}\Gamma_{j,s} &= \frac{\Gamma^0_{j,s}}{1-A_{j,s}\chi^0_{\rm ph}},\\ \Gamma_{j,c} &= \frac{\Gamma^0_{j,c}}{1-A_{j,c}\chi^0_{\rm ph}},\\ \Gamma_{j,{\rm SC}} &= \frac{\Gamma^0_{j,{\rm SC}}}{1-A_{j,{\rm SC}}\chi^0_{\rm pp}},\end{aligned} \tag{28}$$

where $j = 1, \ldots, 3$. We find

$$A_{1,s} = g_4 + 2g_1, \quad A_{2,s} = A_{3,s} = g_4 - g_1,$$
$$A_{1,c} = -g_4 + 2g_1 - 4g_2,$$
$$A_{2,c} = A_{3,c} = -g_4 - g_1 + 2g_2,$$
$$A_{1,\mathrm{SC}} = -g_4 - 2g_3, \quad A_{2,\mathrm{SC}} = A_{3,\mathrm{SC}} = -g_4 + g_3. \quad (29)$$

We see that the Fermi-liquid state becomes unstable when $A_{j,i}\chi^0_{\mathrm{pp(ph)}} = 1$, i.e., at $T \sim |A_{j,i}|^{1/\kappa}$ for small g_i. As χ^0_{pp} and χ^0_{ph} are of the same order, the type of the leading instability, i.e., whether it is superconducting or Pomeranchuk-type, and for which j, depends on the bare values of the couplings $g_1, \ldots, g_4$.

In the ladder approach, we consider each channel independently. This is the legitimate approximation if $A\chi^0$ in one particular channel is much larger than in other channels. However, in our case, the susceptibilities in the particle-particle and the particle-hole channel are of the same order. In this situation, the diagrams that couple different channels are of the same order as the ladder diagrams, and cannot be neglected. Then we have to account for the mutual influence of fluctuations in different channels to correctly describe the low-energy behavior.

V. RENORMALIZATION GROUP

To include the mixing between different channels, we employ a RG approach, in which we keep all leading divergences at each loop order. More formally, in a perturbation expansion the leading diagrams on the n-loop level will be proportional to $T^{n\kappa}$. This includes n-loop diagrams from the different particle-particle and particle-hole ladders, but also mixed diagrams with insertions of a singular l-loop particle-particle contribution into a singular $(n-l)$-loop particle-hole diagram and vice versa ($l < n$). The RG procedure approximates these mixed contributions by the product of decoupled l-loop particle-particle and $(n-l)$-loop particle-hole diagrams (or vice versa). The analogous approximation appears for mixed diagrams of crossed and direct particle-hole type. While this reproduces the correct temperature dependence, or, more generally, the dependence on the RG scale, it introduces an inaccuracy in the prefactor of the mixed diagrams as typical moments in both channels are comparable, and the decoupling is justified only for the order-of-magnitude analysis. The error is formally controlled by the exponent κ in the sense that for the logarithmic RG for $\kappa \to 0$ the decoupling is justified, to logarithmic accuracy. To estimate the error introduced by the decoupling, we compute the two-loop mixed diagrams and compare them with the RG result in Appendix C. We find that the two are reasonably close to each other. We therefore believe that the renormalization-group approach, albeit approximate for HOVH points, is qualitatively accurate.

A. RG equations

When setting up the RG procedure, it is important to choose a suitable regularization. As we have shown in the previous section, the leading contributions come from bubbles with zero-momentum transfer. It is known that momentum-shell cutoffs can be disadvantageous for processes that involve small-momentum particle-hole fluctuations around the Fermi surface because they suppress these fluctuations by construction [21,22]. In a random-phase approximation treatment, this does not lead to problems, but in the description of the interplay of different ordering tendencies particle-hole fluctuations with small and large momentum are not treated equivalently. While this does not affect the competition of superconductivity and spin-density waves with large typical momentum, it is important in our case, where superconducting tendencies compete with zero-momentum orders. Therefore, we choose an RG scheme in which the temperature regularizes interaction corrections and can be used as flow parameter [21]. Alternatively, one can use a frequency regularization scheme and integrate out modes with frequencies larger than a cutoff [5,22]. Eventually, both approaches yield the same renormalization-group flow equations.

To systematically derive the RG equations, we start from a more general point of view and write down all possible vertex corrections within the patch model. This includes not only the leading processes with characteristic momentum of zero, but also the subleading ones with momentum transfer M_i. The flow equations read

$$\dot{g}_1 = -2\dot{\chi}^M_{\mathrm{pp}} g_1 g_2 + \dot{\chi}^0_{\mathrm{ph}}\left[(N-2)g_1^2 + 2g_1 g_4\right] + \dot{\chi}^M_{\mathrm{ph}}\left[2g_1 g_2 - N_f g_1^2 + (2-N_f)g_3^2\right], \quad (30)$$

$$\dot{g}_2 = -\dot{\chi}^M_{\mathrm{pp}}\left(g_1^2 + g_2^2\right) + \dot{\chi}^M_{\mathrm{ph}}\left(g_2^2 + g_3^2\right) + \dot{\chi}^0_{\mathrm{ph}}\{2g_4[g_1 + (1-N_f)g_2] + (N-2)g_2(2g_1 - N_f g_2)\}, \quad (31)$$

$$\dot{g}_3 = 2\dot{\chi}^M_{\mathrm{ph}} g_3[2g_2 - (N_f - 1)g_1] - \dot{\chi}^0_{\mathrm{pp}}\left[2g_3 g_4 + (N-2)g_3^2\right], \quad (32)$$

$$\dot{g}_4 = \dot{\chi}^0_{\mathrm{ph}}\left[(N-1)\left(g_1^2 + 2g_1 g_2 - N_f g_2^2\right) + (3-N_f)g_4^2\right] - \dot{\chi}^0_{\mathrm{pp}}\left[g_4^2 + (N-1)g_3^2\right], \quad (33)$$

where the dots denote the derivatives with respect to the logarithm of the temperature $t = \ln \Lambda/T$, i.e., $\dot{g}_i = \frac{d}{dt} g_i$ and $\dot{\chi}^X_i = \frac{d}{dt}\chi^X_i$, and $\chi^M_i = \chi^{M_1}_i = \chi^{M_2}_i = \chi^{M_3}_i$ due to rotational symmetry. In our case, the number of patches is $N = 3$, but we keep N as a parameter because the same set of RG equations holds for other cases, e.g., for the square lattice, where $N = 2$. We also introduced the number of fermion flavors N_f to account for additional orbital degrees of freedom. In our case, $N_f = 2$, e.g., $N_f = 4$ has been considered for moiré heterostructures [23]. We note in passing that these three-patch RG equations can be systematically derived from the more general functional RG (FRG) equations, by restricting the possible scattering wave vectors accordingly (see Appendix D). Equations (30)–(33) with $\kappa \to 0$ reproduce the logarithmic equations for CVH points (see Refs. [3,20]).

For $\kappa > 0$, the leading terms in these equations are proportional to $\dot{\chi}^0_{\mathrm{pp}}$ and $\dot{\chi}^0_{\mathrm{ph}}$, which both scale as $T^{-\kappa}$. We express their ratio as

$$d_0 = \chi^0_{\mathrm{ph}}/\chi^0_{\mathrm{pp}}. \quad (34)$$

Equations (19) and (20) yield $d_0 \approx 0.25$. Below, we will use d_0 as a free parameter to keep the equations applicable to other systems with HOVH points. As we said, we neglect subleading terms proportional to χ^M_i in Eqs. (30)–(33). We

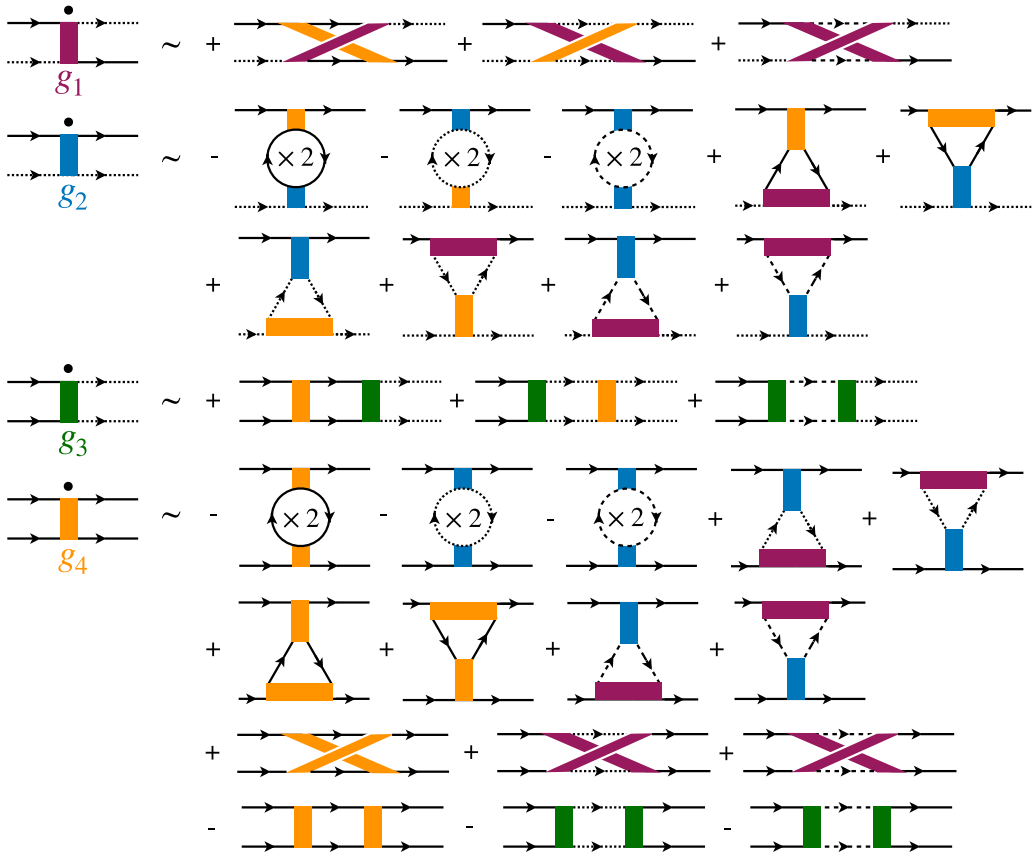

FIG. 6. RG flow equations. Diagrams representing the different RG flow in Eqs. (40)–(43). Note that the two internal lines correspond to the same M point in each diagram. We show the flow equations for three M_p points represented by solid, dashed, and dotted lines.

have checked numerically that the inclusion of constant $\dot{\chi}_i^M$, i.e., logarithmic χ_i^M, does not change the results qualitatively.

B. Dimensionless couplings

Keeping only $\dot{\chi}^0_{\rm pp}$ and $\dot{\chi}^0_{\rm ph}$ in Eqs. (30)–(33) and introducing the dimensionless couplings $\hat{g}_i = g_i \partial_t \chi^0_{\rm pp}$, we obtain the flow equations for the case of N HOVH points:

$$\partial_t \hat{g}_1 = \kappa \hat{g}_1 + d_0\big[(N-2)\hat{g}_1^2 + 2\hat{g}_1\hat{g}_4\big], \tag{35}$$

$$\partial_t \hat{g}_2 = \kappa \hat{g}_2 + 2d_0\hat{g}_4[\hat{g}_1 + (1-N_f)\hat{g}_2] + d_0(N-2)\hat{g}_2(2\hat{g}_1 - N_f\hat{g}_2), \tag{36}$$

$$\partial_t \hat{g}_3 = \kappa \hat{g}_3 - \hat{g}_3[2\hat{g}_4 + (N-2)\hat{g}_3], \tag{37}$$

$$\partial_t \hat{g}_4 = \kappa \hat{g}_4 - \big[\hat{g}_4^2 + (N-1)\hat{g}_3^2\big] + d_0(3-N_f)\hat{g}_4^2 + d_0(N-1)\big(\hat{g}_1^2 + 2\hat{g}_1\hat{g}_2 - N_f\hat{g}_2^2\big). \tag{38}$$

We show a diagrammatic representation in Fig. 6.

For the case of a single HOVH point, the only available coupling is g_4. Setting $g_1 = g_2 = g_3 = 0$, $N = 1$, and $N_f = 2$ in Eq. (38), we reproduce the RG equation in Ref. [17]: $\partial_t \hat{g}_4 = \kappa \hat{g}_4 - (1-d_0)\hat{g}_4^2$. As demonstrated in Ref. [17], this equation has a nontrivial fixed point $\hat{g}_4^* = \kappa/(1-d_0)$, to which the system flows if the bare $\hat{g}_4$ is small enough (see also Ref. [14]). This fixed point describes a critical, metallic ground state—the supermetal—featuring power-law divergent charge and spin susceptibilities, but no long-range spin or charge order.

For more than one HOVH point, we find that the supermetal fixed point becomes unstable. More generally, we searched for fixed points of Eqs. (35)–(38), i.e., solutions with finite $\hat{g}_i$. We find that all fixed points have at least one relevant direction in coupling space, i.e., they are all unstable. The details of the calculation can be found in Appendix E. We will search for fixed trajectories, instead, along which some couplings tend to infinity, indicating an instability of the ordinary metallic state.

C. Flow to strong coupling

In the following, we determine the possible ground states of the system with more than one HOVH point. We focus on our model with $N = 3$ and $N_f = 2$. As a convenient reparametrization we use as flow parameter

$$b = \chi^0_{\rm pp}(T) - \chi^0_{\rm pp}(\Lambda) = \frac{\rho_0 g(\kappa)}{\Lambda^\kappa}\left[\left(\frac{\Lambda}{T}\right)^\kappa - 1\right]. \tag{39}$$

We subtracted from $\chi^0_{\rm pp}(T)$ its value at the UV cutoff Λ so that b ranges from zero at the UV cutoff to infinity in the IR limit. Using this b as the RG scale and returning back to dimensionfull couplings g_i, we obtain the compact flow equations:

$$\partial_b g_1 = d_0\big(g_1^2 + 2g_1g_4\big), \tag{40}$$

$$\partial_b g_2 = 2d_0(g_1 - g_2)(g_4 + g_2), \tag{41}$$

$$\partial_b g_3 = -g_3(2g_4 + g_3), \tag{42}$$

$$\partial_b g_4 = d_0\big[4g_2(g_1 - g_2) + 2g_1^2 + g_4^2\big] - \big(g_4^2 + 2g_3^2\big). \tag{43}$$

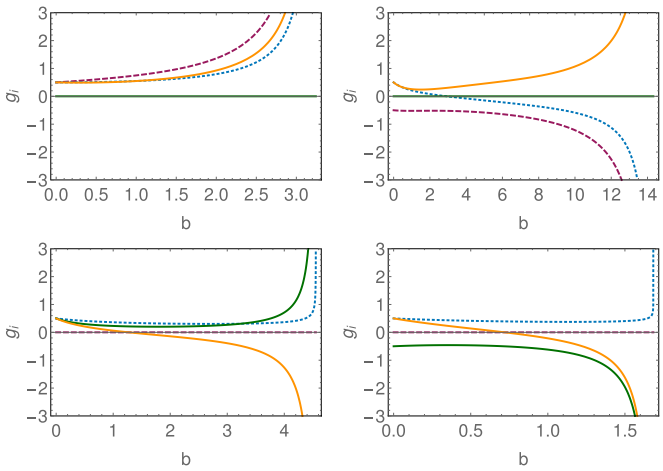

FIG. 7. Flow to strong coupling. Integration of the flow in Eqs. (40)–(43) for four sets of bare couplings and $d_0 = 0.25$. The bare values are $g_1^0 = g_2^0 = g_4^0 = 0.5$, $g_3^0 = 0$ (top left), $-g_1^0 = g_2^0 = g_4^0 = 0.5$, $g_3^0 = 0$ (top right), $g_2^0 = g_3^0 = g_4^0 = 0.5$, $g_1^0 = 0$ (bottom left), and $g_2^0 = -g_3^0 = g_4^0 = 0.5$, $g_1^0 = 0$ (bottom right). g_1, dashed purple; g_2, dotted blue; g_3, solid green; g_4, solid orange.

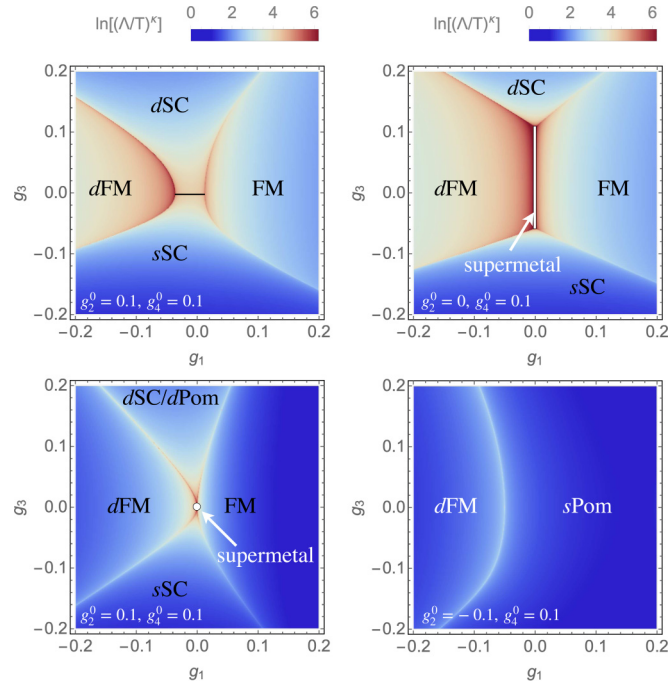

FIG. 8. Phase diagrams. Bare interactions $g_2^0 = g_4^0$ are held fixed and g_1 and g_3 are varied, $d_0 = 0.25$ (top) and $d_0 = 1$ (bottom). Bare values are $g_2^0 = g_4^0 = 0.1$ (left) or $g_2^0 = 0$, $g_4^0 = 0.1$ (right, top), and $g_2^0 = -0.1$, $g_4^0 = 0.1$ (right, bottom). The coloring encodes the scale where the couplings diverge, i.e., where correlations grow strong. If it is too large, e.g., in the red regime, there is no instability or it only occurs at the lowest scales. This can be used to estimate phase boundaries. FM, ferromagnet; dFM, d-wave spin Pomeranchuk; sPOM, s-wave charge Pomeranchuk; dPOM, d-wave charge Pomeranchuk; sSC, s-wave superconductivity; dSC, d-wave superconductivity.

The solution of this equation is shown graphically in Fig. 7. We see that the running couplings diverge at a critical scale b_c, which signals an instability towards an ordered ground state. Below, we discuss which instability develops first. To reach the supermetal state, we have to fine tune the bare values. For example, we can set bare $g_1 = g_2 = 0$ and keep the bare g_3 within certain limits (see Fig. 8). In this case, the couplings g_1 and g_2 remain zero, and g_3 and g_4 flow to zero as T^κ. This means that the corresponding, rescaled dimensionless couplings $\hat{g}_{3,4} = \kappa g_{3,4} \chi_{\rm pp}^0$ approach fixed-point values. Once the bare g_1 and/or g_2 are finite, the flow of the couplings is as in Fig. 7.

Note that we did not include the self-energy corrections into our RG equations. The reason is that the contributions from the self-energy are subleading in their temperature dependence because the first nonanalytic contribution to the self-energy $\Sigma(T) \propto T^{1-2\kappa}$ appears at the two-loop order. One can check that including such a self-energy into the diagrams for the renormalization of g_i will only give rise to subleading terms. Still, self-energy corrections can be relevant because they renormalize the chemical potential and can be expected to generate some additional quadratic momentum dependence in both directions of deviations from the Van Hove points. Both effects spoil the HOVH behavior. We absorb the renormalization of the chemical potential into the effective μ, which we tune to the HOVH point. We also assume that the scale b_c, at which the couplings diverge, is smaller than the one at which the momentum dependence, induced by the self-energy, becomes relevant.

D. Fixed trajectories

When the couplings run into a singularity, they do so in a specific way, where the ratios of the couplings tend to finite values. This is called a fixed trajectory (FT). In general, there are several stable FTs, and it depends on the bare couplings which one the system approaches. Along a FT, the solutions of the RG equations follow the behavior

$$g_i = G_i/(b_c - b). \tag{44}$$

Solving the algebraic equations for G_i, we find different FTs. We are interested in *stable* FTs, to which the system flows under the RG for a range of bare couplings, i.e., without fine tuning. We find eight such stable trajectories for general d_0 (see Table I). For $d_0 \approx 0.25$, we can reach FTs I–IV. We show the flow to these FTs in Fig. 7. When the UV cutoff is such that $d_0 \sim 1$, i.e., the susceptibilities in particle-hole and particle channels are about the same, FTs V and VIII also become available, while FT IV becomes unstable.

E. RG-enhanced susceptibilities

Next, we use the information about the fixed trajectories to study how the susceptibilities for different ordering tendencies behave. To that end, we again introduce the trial vertices $\hat{\Gamma}_i$ in superconducting, and spin and charge $q = 0$ channels ($i \in \{\mathrm{SC}, s, c\}$). We rewrite Eq. (27) as a differential equation, i.e.,

$$\partial_b \hat{\Gamma}_i = \hat{A}_i \hat{\Gamma}_i, \tag{45}$$

where $\hat{A}_i$ are the 3×3 matrices still given by Eq. (27), but the couplings now are the running ones—the solutions of the RG Eqs. (40)–(43), which include the contributions from mixed diagrams.

TABLE I. Fixed trajectories. For convenience, we introduced the abbreviations $D_1 = \sqrt{d_0(12+13d_0)}$, $D_3 = \sqrt{9+8d_0}$, $D_5 = \sqrt{d_0(13d_0-4)}$, and $D_7 = \sqrt{d_0(-24d_0^2+85d_0-36)}$. See Fig. 8 for abbreviations of instabilities.

FT	Range of stability	G_1	G_2	G_3	G_4	Instability
I	No restriction	$\frac{-1+D_1}{d_0(13d_0-1)}$	$G_1/2$	0	$\frac{13d_0-D_1}{2d_0(13d_0-1)}$	FM
II	$d_0 > 1/13 \approx 0.077$	$\frac{-1-D_1}{d_0(13d_0-1)}$	$G_1/2$	0	$\frac{13d_0+D_1}{2d_0(13d_0-1)}$	d-FM
III	$d_0 < \frac{1}{16}(19+\sqrt{73}) \approx 1.73$	0	0	$\frac{d_0-D_3}{9-d_0}$	$-\frac{4}{9+D_3}$	s-SC
IV	$d_0 < \frac{1}{16}(19-\sqrt{73}) \approx 0.65$	0	0	$\frac{d_0+D_3}{9-d_0}$	$-\frac{4}{9-D_3}$	d-SC
V	$d_0 > \frac{1}{6}(9-\sqrt{33}) \approx 0.54$	0	$\frac{-1+2d_0-D_5}{2d_0(1+3d_0)}$	0	$\frac{-5d_0+D_5}{2+6d_0}$	s-POM
VI	$d_0 > \frac{1}{6}(9+\sqrt{33}) \approx 2.46$	0	$\frac{-1+2d_0+D_5}{2d_0(1+3d_0)}$	0	$\frac{-5d_0-D_5}{2+6d_0}$	d-POM
VII	$0.49 \lesssim d_0 \lesssim 0.54$ $1.72 \lesssim d_0 \lesssim 3.05$	0	$\frac{-9+10d_0-D_7}{6d_0(3+d_0)}$	$\frac{4d_0-3d_0^2-D_7}{3d_0(3+d_0)}$	$\frac{-13d_0+D_7}{6d_0(3+d_0)}$	s-POM s-SC/d-POM
VIII	$0.65 \lesssim d_0 \lesssim 2.45$	0	$\frac{-9+10d_0+D_7}{6d_0(3+d_0)}$	$\frac{4d_0-3d_0^2+D_7}{3d_0(3+d_0)}$	$\frac{-13d_0-D_7}{6d_0(3+d_0)}$	d-SC/d-POM

Solving Eq. (45), we find that the eigenvectors $\Gamma_{j,i}$, $j \in \{1,2,3\}$ diverge as $(b_c-b)^{-\beta_{j,i}}$, where the exponents $\beta_{j,i}$ are expressed via the parameters G_1, G_2, G_3, G_4 characterizing the fixed trajectories. Out of the three $\Gamma_{j,i}$ for each i, $\Gamma_{1,i} \propto (1,1,1)$ corresponds to s-wave symmetry, and $\Gamma_{2,i} \propto (0,1,-1)$ and $\Gamma_{3,i} \propto (1,-1/2,-1/2)$ correspond to d-wave symmetry. For the latter, the exponents are degenerate [3,24]. We label the exponents as $\beta_{1,i} = \beta_i^{(s)}$ and $\beta_{2,i} = \beta_{3,i} = \beta_i^{(d)}$ and find

$$\beta_s^{(s)} = d_0(G_4 + 2G_1), \tag{46}$$

$$\beta_s^{(d)} = d_0(G_4 - G_1), \tag{47}$$

$$\beta_c^{(s)} = d_0(-G_4 + 2G_1 - 4G_2), \tag{48}$$

$$\beta_c^{(d)} = d_0(-G_4 - G_1 + 2G_2), \tag{49}$$

$$\beta_{\mathrm{SC}}^{(s)} = -G_4 - 2G_3, \tag{50}$$

$$\beta_{\mathrm{SC}}^{(d)} = -G_4 + G_3. \tag{51}$$

The corresponding susceptibilities behave like

$$\chi_{j,i} \propto \int db\, \Gamma_{j,i}^2 \propto (b_c - b)^{1-2\beta_{j,i}} \tag{52}$$

(see Refs. [25–29] for earlier discussions on this issue). The leading instability at $b = b_c$ will be into the ordered state for which $\beta_{j,i}$ is the largest. Comparing the exponents on different fixed trajectories (see Appendix F), we find that the following orders develop, depending on the bare couplings: (I) ferromagnetism; (II) d-wave spin Pomeranchuk order; (III) s-wave superconductivity; (IV) d-wave superconductivity; (V) s-wave charge Pomeranchuk order; (VI) d-wave charge Pomeranchuk order; (VII) for $0.49 \lesssim d_0 \lesssim 0.54$ s-wave charge Pomeranchuk, for $1.72 \lesssim d_0 \lesssim 2.41$ s-wave superconductivity, for $2.41 \lesssim 3.05$ d-wave charge Pomeranchuk order; and (VIII) for $0.65 \lesssim d_0 < 1$ d-wave superconductivity, and for $1 < d_0 \lesssim 2.45$ d-wave charge Pomeranchuk order. Based on this analysis, we can now determine the phase diagram by solving the flow equations for various bare couplings. The result is shown in Fig. 8. We consider different ranges of the bare couplings to map out all possible instabilities. For a specific lattice model with onsite interaction U, nearest-neighbor interaction V, and nearest-neighbor spin exchange J on the honeycomb lattice, we obtain $g_1^0 = U - V/2 - J$, $g_2^0 = U + 3V/2 - J$, $g_3^0 = U - V/2 + J$, and $g_4^0 = U + 3V/2 - 3J$. However, note that the bare values of the patch model can be altered from the microscopic interactions due to modes with energies higher than the UV cutoff.

We find that for purely repulsive bare couplings the leading instabilities for $d_0 \sim 0.25$ are ferromagnetism and d-wave superconductivity. Superconductivity is driven by the pair-hopping term g_3, which needs to be sufficiently larger than g_1. For larger d_0, the ferromagnetic region grows. For $d_0 > 1$, d-wave superconductivity is replaced by d-wave charge Pomeranchuk order.

In case some couplings become attractive, we find an s-wave pairing, charge Pomeranchuk order, and a tendency towards a d-wave spin Pomeranchuk order. In fact, only a small negative g_1 is needed to induce the d-wave spin Pomeranchuk order. We also find the supermetal phase [17], where couplings do not diverge in our phase diagram. However, as we explained in Sec. V A, the bare couplings must be tuned to certain values to reach this phase (see Fig. 8).

VI. FREE ENERGY FOR d-WAVE ORDERS

Within the RG analysis, the exponents in the d-wave channels $\beta_{2,i}$ and $\beta_{3,i}$ are equal. Hence, the system simultaneously becomes unstable towards the order with the structure set by the (normalized) $\Gamma_2 = 1/\sqrt{2}(0,1,-1)$ and $\Gamma_3 = \sqrt{2/3}(1,-1/2,-1/2)$. The corresponding order parameters are commonly called d_{xy} and $d_{x^2-y^2}$ due to their symmetry. To determine which combination of the d_{xy} and $d_{x^2-y^2}$ orders develops, one needs to analyze the Landau free energy.

For a SC order, we introduce $\Delta_{\mathrm{SC}} = \Delta_2\Gamma_2 + \Delta_3\Gamma_3$. Both Δ_1 and Δ_2 are $U(1)$ complex order parameters. The free energy is of the form

$$\mathcal{F}_{d\mathrm{SC}} = \frac{\alpha}{2}(|\Delta_2|^2 + |\Delta_3|^2) + \beta_1(|\Delta_2|^2 + |\Delta_3|^2)^2 + \beta_2\left|\Delta_2^2 + \Delta_3^2\right|^2. \tag{53}$$

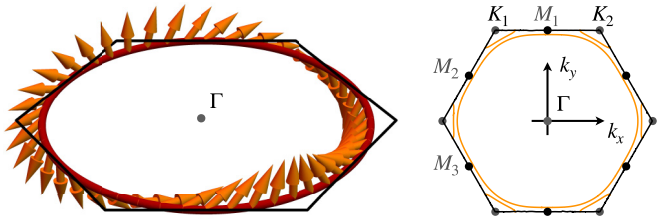

FIG. 9. d-wave spin Pomeranchuk order. Left panel: The order parameter of the d-wave spin Pomeranchuk order winds twice around the Fermi surface. Right panel: Diagonalization leads to a Zeeman-like term without net magnetization which splits the Fermi surface.

The coefficient α changes sign at the transition. We verified that for a HOVH point $\beta_1, \beta_2 > 0$, like for the case of a CVH point in graphene [3]. In this case, the combination $\Delta_3 = \pm i\Delta_2$ minimizes the free energy, i.e., $\Delta_{\rm SC} = (\Gamma_2 \pm i\Gamma_3)\Delta$ with complex Δ. This is a chiral $d \pm id$ superconducting state [7].

For d-wave charge Pomeranchuk order, we introduce two real order parameters φ_2 and φ_3 and the total order parameter is $\varphi_c = \varphi_2\Gamma_2 + \varphi_3\Gamma_3$. A hexagonal lattice allows for a cubic term in the free energy [30–35]. Keeping this term and neglecting φ^4 terms, we obtain

$$\mathcal{F}_{d\rm POM} = \frac{\bar{\alpha}}{2}\left(\varphi_2^2 + \varphi_3^2\right) + \bar{\beta}\left(\varphi_3^3 - 3\varphi_3\varphi_2^2\right). \tag{54}$$

Minimizing the free energy (including quartic terms), we find that the system chooses one out of three equivalent states: either $\varphi_c \propto (2, -1, -1)$, $\varphi_c \propto (-1, 2, -1)$, or $\varphi_c \propto (-1, -1, 2)$. Each state selects one particular HOVH point where the order is largest. Such a state breaks lattice C_3 rotational symmetry and is a charge nematic [30–35].

For the d-wave spin channel, we express the order parameter via $O(3)$-symmetric vectors $\vec{\phi} = \vec{\phi}_2\Gamma_2 + \vec{\phi}_3\Gamma_3$ (ϕ_i and Γ_i live in different vector spaces). The cubic term is absent and the free energy up to quartic order in $\vec{\phi}_{2,3}$ is given by the expression

$$\mathcal{S}_{d\rm FM} = \frac{\tilde{\alpha}}{2}\left(\vec{\phi}_1^2 + \vec{\phi}_2^2\right) + \frac{\tilde{\beta}}{2}\left[\left(\vec{\phi}_1^2 + \vec{\phi}_2^2\right)^2 - \frac{4}{3}\vec{\phi}_1^2\vec{\phi}_2^2 + \frac{4}{3}(\vec{\phi}_1 \cdot \vec{\phi}_2)^2\right]. \tag{55}$$

The coefficient $\tilde{\beta}$ is obtained by integrating out the fermions near a HOVH point. We find a positive result, reading

$$\tilde{\beta} = \int G^4 = T\sum_{\omega}\int d\epsilon \frac{\rho(\epsilon)}{6}\partial_\epsilon^3 \frac{1}{i\omega - \epsilon} \tag{56}$$

$$= \frac{\rho_0}{48}T^{-(2+\kappa)}\int du \frac{2 - \cosh u}{|u|^\kappa \cosh^4\left(\frac{u}{2}\right)} > 0. \tag{57}$$

For $\kappa = 1/4$, we have $\beta \approx 0.96/T^{9/4}$. Minimizing the free energy, we find that both $\vec{\phi}_2$ and $\vec{\phi}_3$ are nonzero. Specifically, $|\vec{\phi}_2| = |\vec{\phi}_3| = |\vec{\phi}|$, and $\vec{\phi}_2$ and $\vec{\phi}_3$ are perpendicular to each other. Combining this with the d-wave modulation, and extending the modulation to the full Fermi surface, we find that the spin order parameter winds twice around the Fermi surface. We illustrate this in Fig. 9. This order breaks $SU(2)$ spin symmetry, but does not generate net magnetization due to the d-wave form factor.

To see the effect of the d-wave spin Pomeranchuk order on the energy dispersion, we consider the mean-field Hamiltonian

$$H_{\rm MF} = \sum_{p\sigma}\epsilon(\vec{p})c_{p\sigma}^\dagger c_{p\sigma} + g_{s,d}\sum_{p\sigma,\sigma'}\vec{\phi}(\vec{p})c_{p\sigma}^\dagger\vec{\sigma}_{\sigma\sigma'}c_{p\sigma'}, \tag{58}$$

with free energy dispersion $\epsilon(\vec{p})$ and coupling $g_{s,d}$. We express the order parameter $\vec{\phi}(\vec{p})$ as $\vec{\phi}(\vec{p}) = d_{xy}(\vec{p})\hat{\phi}_2 + d_{x^2-y^2}(\vec{p})\hat{\phi}_3$, where $\hat{\phi}_2$ and $\hat{\phi}_3$ are orthogonal order parameters and $d_{xy}(\vec{p})$ and $d_{x^2-y^2}(\vec{p})$ are the momentum-dependent d-wave form factors $d_{xy} = \sin 2\theta_p$ and $d_{x^2-y^2} = \cos 2\theta_p$ with the polar angle θ_p.

$H_{\rm MF}$ is nondiagonal in the spin index. Diagonalization leads to the reconstructed energy bands

$$E(\vec{k}) = \epsilon(\vec{k}) - \mu \pm |\vec{\phi}|. \tag{59}$$

We see that the d-wave spin Pomeranchuk order introduces a Zeeman-like splitting (see Fig. 9), which is, however, not spin polarized. In real space, the d-wave form factor translates to a modulation of the nearest-neighbor hopping. As $\vec{\phi}$ couples to the electron spin [see Eq. (58)], the hopping becomes spin dependent.

VII. CONCLUSION

We presented an analysis of competing instabilities for a system of interacting electrons in the presence of multiple HOVH points. At a HOVH point, the density of states diverges by a power law, and we have shown that this gives rise to a qualitatively new type of competition between superconducting and zero-momentum particle-hole orders. Our analysis of particle-particle and particle-hole susceptibilities has revealed that the ones with zero-momentum transfer diverge by a power law, with the same exponent in the particle-particle and the particle-hole channel, while the ones at a finite momentum transfer diverge at most logarithmically. This is in sharp contrast to CVH points, where the divergences are logarithmic, and the susceptibilities in the particle-hole channel are either subleading to the ones in the particle-particle channel or are comparable, but at finite momentum transfer, if the Fermi surface is nested.

We argued that the physics associated with multiple HOVH points in the Brillouin zone is relevant for intercalated graphene, where Van Hove filling has recently been achieved experimentally. It was observed that near this filling the band dispersion is strongly flattened around the Van Hove points [10]. HOVH points also appear in, e.g., twisted bilayer graphene, where they can be accessed by single-parameter tuning [12].

To model the HOVH scenario in graphene-based systems, we introduced a tight-binding model on the honeycomb lattice with up to third-nearest-neighbor hopping and tuned the hopping amplitudes such that higher-order saddle points appear at the three inequivalent M points in the Brillouin zone. We derived the effective patch model for electrons around the HOVH points, which includes couplings for all symmetry-allowed scattering processes. To analyze the competition between different ordering channels in an unbiased

way, we set up the renormalization-group approach that accounts for all leading fluctuation corrections. The patch model and the renormalization-group equations are valid for both hexagonal and tetragonal systems with HOVH points at the Brillouin-zone edges.

We have shown that the supermetal state, which was predicted to be the ground state for a single HOVH point, is unstable when several HOVH points are present. It can only survive under special fine-tuned conditions for the initial couplings. For generic initial conditions, we observed a flow to strong coupling, indicating that an initial Fermi-liquid state becomes unstable towards a symmetry-broken ordered state. We obtained the phase diagram for parameters relevant for intercalated graphene. It includes regions of ferromagnetism, charge and spin Pomeranchuk orders, as well as s- and d-wave superconductivity. The development of a specific instability depends on model parameters, i.e., the bare couplings and the ratio of the particle-particle and the particle-hole susceptibilities. For purely repulsive interactions, we found that two key competitors are ferromagnetism and chiral $d+id$ superconductivity. We note that slightly away from Van Hove filling spin-triplet f-wave superconductivity can also become a competitor [4,6,13,36,37]. We expect this tendency to be stronger in the vicinity of HOVH points because of increased ferromagnetic fluctuations. If some interactions turn attractive, s-wave superconductivity can develop. In addition, we found that under some initial conditions the system develops d-wave charge or spin Pomeranchuk order. We analyzed the free energy for the d-wave Pomeranchuk orders to determine the ground-state configurations. We found that the d-wave charge Pomeranchuk order breaks lattice rotational symmetry. For the d-wave spin Pomeranchuk order, we found that the order parameter winds twice around the Fermi surface. Such an order is very unconventional: it breaks spin $SU(2)$ symmetry and splits the Fermi surface, but it does not introduce a net magnetization. Our results demonstrate that the many-body phase diagram of intercalated graphene and similar systems is very rich and hosts not only chiral superconductivity but also unconventional spin and charge orders.

In future work, it will be interesting to improve our RG procedure regarding self-energy corrections or the approximation error of the mixed diagrams, by, e.g., employing functional RG techniques with more sophisticated truncations. Another future research direction is to adapt our formalism to systems that possess HOVH points in different locations of the Brillouin zone. One straightforward application is to the case of twisted bilayer graphene, where three HOVHs lie along the Γ-M line away from the zone boundary [12].

ACKNOWLEDGMENTS

We thank D. V. Chichinadze, D. M. Kennes, Y.-P. Lin, R. Thomale, A. M. Tsvelik, and S. Wessel for valuable discussions. M.M.S. was supported by the Deutsche Forschungsgemeinschaft through Sonderforschungsbereich 1238 (projects C02 and C03, Grant No. 277146847), and C.H. was supported through Research Training Group Grant No. 1995. L.C. was supported by the Humboldt foundation during the first part of the project and by the U.S. Department of Energy, Office of Basic Energy Sciences, under Grant No. DE-SC0012704 during the later part of the project. A.V.C. was supported by the Office of Basic Energy Sciences, U.S. Department of Energy, under Grant No. DE-SC0014402.

APPENDIX A: BAND DISPERSION NEAR THE M POINTS

To demonstrate how the HOVH points come about in our model, we expand the dispersion around the M points. For the expansion at $M_1 = \pi(0, 2/3)$, we obtain

$$\epsilon_{M_1}(\vec{x}) = -a_1x^2 + b_1y^2 + c_1x^4 + d_1y^4 + e_1x^2y^2 + \cdots,$$

where $\vec{x} = (x, y) = (k_x - M_{1,x}, k_y - M_{1,y})$ is the deviation from the corresponding M point and the dots denote higher-order terms in x, y. The coefficients are

$$a_1 = \frac{3}{4}(t_1 - 2t_2 - 4t_3), \tag{A1}$$

$$b_1 = \frac{2t_1^2}{t_1 - 3t_3} + \frac{t_1}{4} + 3t_3 - \frac{9t_2}{2}, \tag{A2}$$

$$c_1 = \frac{3}{64}[t_1 - 2(7t_2 + 8t_3)], \tag{A3}$$

$$d_1 = \frac{3(9t_2 - 8t_3)}{32} + \frac{7t_3t_1^2 - 63t_1^3 + 27t_3^2t_1 + 405t_3^3}{64(t_1 - 3t_3)^3/(3t_1)},$$

$$e_1 = \frac{27}{16}t_2 + \frac{27\left(t_1^3 - 14t_3t_1^2 + 33t_3^2t_1 - 16t_3^3\right)}{32(t_1 - 3t_3)^2}. \tag{A4}$$

The energy dispersion near the other M points, $M_2 = \pi(-1/\sqrt{3}, 1/3)$ and $M_3 = -\pi(1/\sqrt{3}, 1/3)$, is

$$\epsilon_{M_2}(\vec{x}) = a_2x^2 + c_2xy + b_2y^2 + \cdots, \tag{A5}$$

$$\epsilon_{M_3}(\vec{x}) = a_3x^2 + c_3xy + b_3y^2 + \cdots, \tag{A6}$$

where $\vec{x}$ is again measured from the corresponding M point and the coefficients are

$$a_2 = a_3 = \frac{3t_1^2}{2(t_1 - 3t_3)} - 3t_2 + 3t_3, \tag{A7}$$

$$b_2 = b_3 = \frac{9(t_1 - 2t_3)t_3}{2(t_1 - 3t_3)}, \tag{A8}$$

$$c_2 = -c_3 = -\frac{3\sqrt{3}[t_1^2 - (2t_2 + t_3)t_1 + 6t_2t_3]}{2(t_1 - 3t_3)}. \tag{A9}$$

1. High-order saddle point

We note that the quadratic term $\propto x^2$ in Eq. (4) can be tuned to zero by choosing

$$t_3 \to t_{3,e} = (t_1 - 2t_2)/4. \tag{A10}$$

In that case, the usual saddle point is replaced by an even flatter energy dispersion. More explicitly, the band dispersion near M_1 then reads

$$\epsilon_{M_1}(\vec{x})\big|_{t_{3,e}} = \bar{b}_1y^2 - \bar{c}_1x^4 - \bar{e}_1x^2y^2 + \ldots, \tag{A11}$$

where we have introduced

$$\bar{b}_1 = t_1 - 6t_2 + \frac{8t_1^2}{t_1 + 6t_2}, \tag{A12}$$

$$\bar{c}_1 = \frac{9}{64}(t_1 + 2t_2), \tag{A13}$$

$$\bar{e}_1 = \frac{27(t_1 + 2t_2)\left(11t_1^2 - 28t_1t_2 - 52t_2^2\right)}{32(t_1 + 6t_2)^2}. \tag{A14}$$

For these parameters we not only have $\nabla_{\vec{x}}\epsilon_{M_1}(\vec{x}) = 0$ at the saddle point, but also the Hessian matrix $H_{ij} = \partial_{x_i}\partial_{x_j}\epsilon_{M_1}(\vec{x})$ has a vanishing determinant, i.e., $\det H(\vec{x}) = 0$. The higher-order saddle point is shown in Fig. 3.

2. Density of states

At such a two-dimensional higher-order saddle point, the DOS shows a power-law divergence:

$$\rho(\epsilon) \propto |\epsilon|^{-\kappa}, \tag{A15}$$

with some exponent $\kappa > 0$. This divergence is stronger than the logarithmic one at a CVH singularity. The singular behavior of the DOS near the high-order saddle point can be determined from a scaling argument [18]. To that end, the Taylor expanded dispersion $\epsilon_{M_1}(\vec{x})$ is decomposed into two parts, the canonical part $\epsilon_c(\vec{x})$ and a perturbation $\epsilon_p(\vec{x})$, i.e., $\epsilon_{M_1}(\vec{x}) = \epsilon_c(\vec{x}) + \epsilon_p(\vec{x})$. The canonical part has vanishing gradient and is defined by being scale invariant:

$$\epsilon_c(\lambda^p x, \lambda^q y) = \lambda\epsilon_c(x, y). \tag{A16}$$

The perturbation part can, again, be decomposed into monomials with individual scaling behavior reading

$$\epsilon_p(\lambda^p x, \lambda^q y) = \lambda^r\epsilon_p(x, y). \tag{A17}$$

The perturbation is irrelevant at the HOVH point for $r > 1$ and relevant for $r < 1$. In our present scenario, we have

$$\epsilon_c(x, y) = -\bar{c}_1x^4 + \bar{b}_1y^2 \Rightarrow\ p = 1/4, \quad q = 1/2, \tag{A18}$$

$$\epsilon_p(x, y) = -\bar{e}_1x^2y^2 + \ldots, \tag{A19}$$

so the scaling exponent of the monomial $\propto \bar{e}_1$ is $r = 3/2 > 1$ and therefore it is irrelevant along with all higher-order terms. Using the canonical dispersion, the scale invariance, and the definition of the DOS $\rho(\epsilon) = \int_{\vec{x}} \delta[\epsilon - \epsilon_c(\vec{x})]$, one can show that the DOS is also scale invariant:

$$\rho(\lambda\epsilon) = \lambda^\kappa\rho(\epsilon), \tag{A20}$$

with $\kappa = p + q - 1$ and p, q as determined above. Then, the singular part of the DOS behaves according to

$$\rho(\epsilon) \propto |\epsilon|^\kappa \propto |\epsilon|^{-\frac{1}{4}}, \tag{A21}$$

i.e., in our model $\kappa = 1/4$.

APPENDIX B: NUMERICAL EVALUATION OF THE LOOPS

We confirm the hierarchy of particle-particle and particle-hole bubbles that we obtained through expansion around the Van Hove points by numerical evaluation of the loops in the full Brillouin zone with the microscopic dispersion. We use the third-neighbor hopping as the tuning parameter to change from a logarithmic divergence to a power-law divergence at the Van Hove points. Figure 10 shows the temperature dependence of $\partial_t\chi^X_{\mathrm{pp/ph}}$ [Eq. (17)] for two cases: an almost perfectly nested situation with $t_3 = 0.01t_1$ and the situation with an HOVHS for $t_3 = t_1/4$ ($t_2 = 0$ in both cases). Because we plot the loop derivatives against the logarithm of the temperature $t = \ln\Lambda/T$, we expect a linear behavior for the derivatives of $\ln^2$-divergent bubbles, i.e., χ^0_{pp} and χ^M_{ph}, and a constant for the derivatives of ln-divergent bubbles, i.e., χ^M_{pp} and χ^0_{ph} in the nested case. Furthermore, a finite t_3 destroys nesting at the lowest scales, so that the growth of χ^M_{ph} is stopped. In the case with the eVHS, we expect the particle-particle bubble with zero incoming momentum and the particle-hole bubble with zero-momentum transfer to grow like a power law, which is an exponential when plotted against $t = \ln\Lambda/T$. This is exactly what we find, in agreement to the approximate analytical calculation Eqs. (20) and (19). This confirms that there is a qualitative change in the loop hierarchy with χ^0_{pp} and χ^0_{ph} growing large at small temperatures while the other loops become subleading. In Fig. 11, we show how this hierarchy changes when t_3 is varied. We can also extract an estimate for the parameter d_0 when we compare the magnitude of $\dot{\chi}^0_{\mathrm{pp}}$ and $\dot{\chi}^0_{\mathrm{ph}}$. We obtain a similar value as before: $d_0 \approx 0.30$.

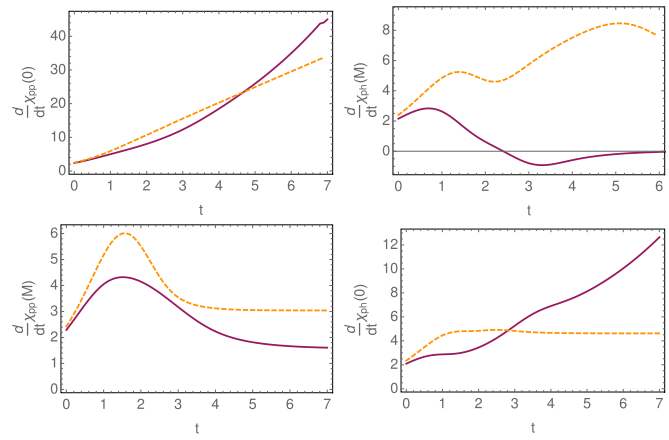

FIG. 10. Temperature derivative of loop corrections. We plot $d/dt\,\chi^X_{\mathrm{pp}}$ and $d/dt\,\chi^X_{\mathrm{ph}}$ [see Eqs. (17) and (18) with $t = \ln\Lambda/T$ for the microscopic model Eq. (1)]. From left to right and top to bottom, we show $d/dt\,\chi^0_{\mathrm{pp}}$, $d/dt\,\chi^M_{\mathrm{ph}}$, $d/dt\,\chi^M_{\mathrm{pp}}$, and $d/dt\,\chi^0_{\mathrm{ph}}$. As an example for the situation with a HOVH singularity we chose $t_3 = t_1/4, t_2 = 0$ (solid, purple). For comparison, we also show the case with a logarithmic DOS for $t3 = 0.01t_1, t_2 = 0$ (dashed, yellow). When plotted as a function of the logarithmic temperature t, $\chi^X_i \propto (\Lambda/T)^\kappa$ leads to an exponential growth as observable in χ^0_{pp} and χ^0_{ph} (solid, purple). The logarithmic singularity $\chi^X_i \propto \ln^2\Lambda/T$ leads to a linear behavior in the derivative as observable for χ^0_{pp} and χ^M_{ph} (dashed, yellow). The linear growth in χ^M_{ph} is cut for small enough temperatures $t \gtrsim 5$ due to imperfect nesting $t_3 = 0.01t_1$.

APPENDIX C: RG VS PERTURBATION EXPANSION

To verify the accuracy of the RG equations, it is instructive to compare it with a direct perturbative computation of the renormalization of the couplings. A straightforward comparison shows that our RG approach reproduces the correct temperature dependence and the prefactors of the

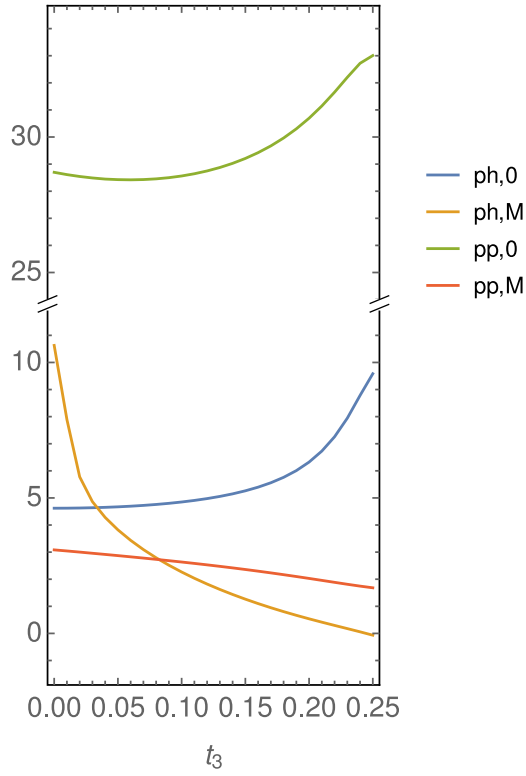

FIG. 11. Loop derivatives $\partial_t \chi^X_{\mathrm{pp/ph}}$ as a function of t_3 for a fixed (arbitrary) temperature $t = \ln \Lambda/T = 5.8$.

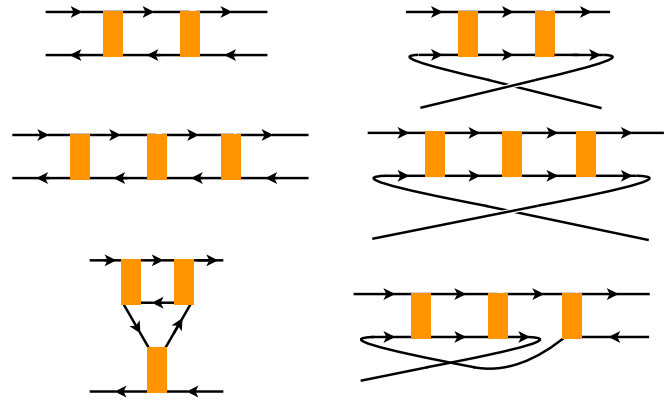

FIG. 12. Exemplary diagrams at one- and two-loop level if $g_1 = g_2 = g_3 = 0$. Diagrams can be classified into three channels, often denoted as crossed particle-hole, particle-particle, and direct particle-hole channel. On the one-loop level (first line), we have contributions from the crossed particle-hole and the particle-particle channel. Diagrams in the direct particle-hole channel cancel against each other. On the two-loop level, we can distinguish pure diagrams, which consist only of contributions belonging to the same channel, and mixed diagrams, which contain subdiagrams from different channels. The second line contains pure diagrams in the crossed particle-hole and the particle-particle channel. The last line shows examples of mixed diagrams: a mixed crossed and direct particle-hole (left) and a mixed particle-particle and particle-hole diagram (right). The RG approximates the mixed diagrams as the product of its subdiagrams.

contributions coming from the ladder diagrams, and that it also contains contributions, which in perturbation theory come from the diagrams which contain segments with particle-particle and particle-hole bubbles. However, these last contributions are not reproduced exactly within our RG. Specifically, the power-law forms of the temperature dependencies are captured correctly, but the prefactors are reproduced only up to corrections of order 1. In the limit of $\kappa \to 0$, i.e., for the logarithmic RG, these deviations vanish; i.e., to logarithmic accuracy, RG exactly reproduces perturbation theory order by order.

To exemplify this, we compare the expressions, obtained from the RG and from the direct perturbation expansion up to two-loop order. For clarity, we simplify the problem and set $g_1 = g_2 = g_3 = 0$, i.e., we consider the case when only the g_4 coupling is nonzero (with our RG, if bare $g_1 = g_2 = g_3 = 0$, the dressed couplings also vanish). Then, the RG equation for g_4 is

$$\partial_b g_4 = (d_0 - 1) g_4^2 \tag{C1}$$

[see Eq. (43)]. Solving this equation iteratively, starting from bare g_0, we obtain the following series:

$$g_4 = g_0 + (d_0 - 1) b g_0^2 + \left(d_0^2 - 2d_0 + 1\right) b^2 g_0^3. \tag{C2}$$

Within the diagrammatic perturbation theory, the $O(bg_0^2)$ term comes from the one-loop diagrams, and the $O(b^2 g_0^3)$ term comes from the two-loop diagrams. At one-loop order, the two diagrams describe the renormalization of g^4 by particle-hole and particle-particle bubbles (see Fig. 12). There are bg_0^2 contributions from other diagrams (not shown), but they cancel out. Evaluating these diagrams, we reproduce the prefactor $d_0 - 1$ in Eq. (C2).

We next move to two-loop order. One can identify what kinds of two-loop diagrams would reproduce the three terms of order $b^2 g_0^3$ in Eq. (C2). The power of d_0 indicates that the term $d_0^2 b^2 g_0^3$ is the contribution with two particle-hole bubbles:

$$D^{\mathrm{RG}}_{\mathrm{ph}} = T^2 g_0^3 \sum_{k_0, q_0} \int d\vec{k} \int d\vec{q} G^2(q) G^2(k). \tag{C3}$$

For brevity, we collect Matsubara frequency and momentum as $k = (k_0, \vec{k})$. Here and below we assume that $\vec{q}$ and $\vec{k}$ denote deviations from the M_i point. The term $-2d_0 b^2 g_0^3$ is a mixed particle-particle/particle-hole contribution,

$$D^{\mathrm{RG}}_{\mathrm{pp,ph}} = 2T^2 g_0^3 \sum_{k_0, q_0} \int d\vec{k} \int d\vec{q} G^2(q) G(k) G(-k), \tag{C4}$$

and the term $b^2 g_0^3$ is the contribution from two bubbles in the particle-particle channel:

$$D^{\mathrm{RG}}_{\mathrm{pp}} = T^2 g_0^3 \sum_{k_0, q_0} \int d\vec{k} \int d\vec{q} G(q) G(-q) G(k) G(-k). \tag{C5}$$

Here and below we use that $-\vec{k} - M_i = -\vec{k} + M_i$ (up to the reciprocal-lattice vector), i.e., $\vec{q}$ and $\vec{k}$ also denote deviations from the M_i point in particle-particle bubbles. We see that in all contributions in Eqs. (C3)–(C5) the integration/summation over k and q decouples, i.e., these terms are the products of one-loop diagrams.

In the direct perturbation theory, the perturbative contributions can also be assembled into contributions from

two particle-hole loops, two particle-particle loops, and one particle-hole and one particle-particle loop. Exemplary diagrams (not all), which contribute to the renormalization of g_4 at two-loop order, are shown in Fig. 12.

The two-loop diagram with two particle-particle loops (the top right one in Fig. 12) is the direct product of two one-loop particle-particle diagrams, and it yields the same result as in the RG:

$$D_{\rm pp}^{\rm pert} = g_0^3 T^2 \sum_{k_0,q_0} \int d\vec{k} \int d\vec{q}\; G(q)G(-q)G(-k)G(k) = D_{\rm pp}^{\rm RG}. \tag{C6}$$

In the particle-hole channel, we get two types of diagrams from the perturbation expansion. Diagrams of one type are the ones in which the integration/summation over k and q factorizes (e.g., the top left diagram in Fig. 12). In the diagrams of the other type (e.g., the bottom left one in Fig. 12), there is no factorization. In total, the two-loop particle-hole diagrams sum to

$$D_{\rm ph}^{\rm pert} = 2T^2 g_0^3 \sum_{k_0,q_0} \int d\vec{k} \int d\vec{q}\; G^2(q)G^2(k) - 2T^2 g_0^3 \sum_{k_0,q_0} \int d\vec{k} \int d\vec{q}\; G^2(q)G(k)G(M_i+k-q).$$

Here and below we have set all external frequencies and momenta to be the same, assuming they are located at M points M_i. In the logarithmic case with DOS $\rho(\epsilon) = \rho_0 \ln(\Lambda/\epsilon)$, the main contribution in the coupled integral comes from $\epsilon_k \gg \epsilon_q$ and we can approximate the second integral via

$$\begin{aligned} &T^2 \sum_{k_0,q_0} \int d\vec{k} \int d\vec{q}\; G^2(q)G(k)G(M_i+k-q) \\ &\approx T^2 \sum_{k_0,q_0} \int d\vec{q}\; G^2(q) \int_{\epsilon_k \gtrsim \epsilon_q} d\vec{k}\; G^2(k) \\ &= \int d\epsilon \rho(\epsilon) n_F'(\epsilon) \int_{\epsilon'>\epsilon} d\epsilon' \rho(\epsilon') n_F'(\epsilon') \\ &\approx \rho_0^2 \ln^2(\Lambda/T) \int d\epsilon \frac{1}{4\cosh^2(\epsilon/2)} \int_{\epsilon'>\epsilon} d\epsilon' \frac{1}{4\cosh^2(\epsilon'/2)} \\ &= \frac{1}{2}\left[\rho_0 \ln(\Lambda/T) \int d\epsilon \frac{1}{4\cosh^2(\epsilon/2)}\right]^2 \\ &= \frac{1}{2} T^2 \sum_{k_0,q_0} \int d\vec{q} \int d\vec{k}\; G^2(q)G^2(k). \end{aligned} \tag{C7}$$

Here, we have neglected terms that are smaller than $\ln^2(\Lambda/T)$. Substituting into (C7), we find that the direct perturbation theory yields, to logarithmic accuracy,

$$D_{\rm ph}^{\rm pert} = D_{\rm ph}^{\rm RG}. \tag{C8}$$

However, in the case of the HOVH point, we cannot decouple the integrations over $\mathbf{k}$ and $\mathbf{q}$, i.e., $D_{\rm ph}^{\rm pert} \neq D_{\rm ph}^{\rm RG}$. Thus, there is a difference between the RG and the perturbation expansion.

We show below that this leads to corrections in the prefactor, while the temperature dependence is reproduced correctly, i.e., $D_{\rm ph}^{\rm pert} = c D_{\rm ph}^{\rm RG}$ with a constant $c = \mathcal{O}(1)$.

Finally, the mixed particle-particle/particle-hole diagrams in the perturbation expansion sum to

$$\begin{aligned} D_{\rm pp,ph}^{\rm pert} &= 2T^2 g_0^3 \sum_{k_0,q_0} \int d\vec{k} \int d\vec{q} G^2(q)G(k)G(M_i+q-k) \\ &\quad + 2T^2 g_0^3 \sum_{k_0,q_0} \int d\vec{k} \int d\vec{q} G(q)G(-q) \\ &\quad \times G(k)G(M_i+k+q) \end{aligned} \tag{C9}$$

(see the bottom right diagram in Fig. 12 for an example). The second term in Eq. (C9) becomes subleading in the logarithmic case, because the second logarithm of the particle-particle channel is cut by the particle-hole insertion:

$$\begin{aligned} &T^2 \sum_{k_0,q_0} \int d\vec{q} \int d\vec{k} G(q)G(-q)G(k)G(M_i+k+q) \\ &\approx T^2 \sum_{k_0,q_0} \int d\vec{q} \int_{\epsilon_k \gtrsim \epsilon_q} d\vec{k}\; G(q)G(-q)G^2(k) \\ &= \int d\epsilon \rho(\epsilon) \frac{1-2n_F(\epsilon)}{2\epsilon} \int_{\epsilon'>\epsilon} d\epsilon' \rho(\epsilon') n_F'(\epsilon') \\ &\approx -\rho_0^2 \ln^2(\Lambda/T) \int d\epsilon \frac{\tanh\epsilon/2}{2\epsilon} \int_{\epsilon'>\epsilon} d\epsilon' \frac{1}{4\cosh^2\epsilon'/2} \\ &= \rho_0^2 \ln^2(\Lambda/T) \int d\epsilon \frac{\tanh\epsilon/2}{2\epsilon} \frac{\tanh\epsilon/2 - 1}{2}. \end{aligned} \tag{C10}$$

This contribution is of order $\ln^2(\Lambda/T)$. In contrast, the first term in Eq. (C9) is of order $\ln^3(\Lambda/T)$. Indeed,

$$\begin{aligned} &T^2 \sum_{k_0,q_0} \int d\vec{k} \int d\vec{q} G^2(q)G(k)G(M_i+q-k) \\ &\approx T^2 \sum_{k_0,q_0} \int d\vec{q} \int_{\epsilon_k \gtrsim \epsilon_q} d\vec{k} G^2(q)G(k)G(-k) \\ &= \int d\epsilon \rho(\epsilon) n_F'(\epsilon) \int_{\epsilon}^{\Lambda/T} d\epsilon' \rho(\epsilon') \frac{1-2n_F(\epsilon')}{2\epsilon'} \\ &\approx -\rho_0^2 \ln^2(\Lambda/T) \int d\epsilon \frac{1}{4\cosh^2\epsilon/2} \int_{\epsilon}^{\Lambda/T} d\epsilon' \frac{\tanh\epsilon'/2}{2\epsilon'} \\ &= O[\ln^3(\Lambda/T)]. \end{aligned} \tag{C11}$$

One can verify that, to logarithmic accuracy,

$$\begin{aligned} &T^2 \sum_{k_0,q_0} \int d\vec{k} \int d\vec{q} G^2(q)G(k)G(M_i+q-k) \\ &= T^2 \sum_{k_0,q_0} \int d\vec{q} \int d\vec{k} G^2(q)G(k)G(-k). \end{aligned} \tag{C12}$$

We note that if the calculation is performed at zero temperature and regularized by a nonzero deviation from the Van Hove points, both contributions in Eq. (C9) are of order $\ln^3(\Lambda/T)$, but eventually sum to the same prefactor as the one at a nonzero temperature. So we find that for the logarithmic DOS (the case $\kappa \to 0$)

$$D_{\rm pp,ph}^{\rm pert} = D_{\rm pp,ph}^{\rm RG} \tag{C13}$$

to logarithmic accuracy. For our case of HOVH points, $D^{\text{pert}}_{\text{pp,ph}}$ and $D^{\text{RG}}_{\text{pp,ph}}$ are not equivalent because the integrals over $\mathbf{k}$ and $\mathbf{q}$ do not decouple. Like before, $D^{\text{pert}}_{\text{pp,ph}} = \tilde{c} D_{\text{pp,ph}}$ with $\tilde{c} = \mathcal{O}(1)$. For verification, we explicitly calculate the coupled integrals to show that we still get the correct temperature dependence.

For concreteness, we consider Van Hove filling and $\kappa = 1/4$. We use the dispersions for the vicinity of the M points Eq. (8), i.e., $\epsilon_{\vec{q}} = \epsilon_{M_1}(\vec{q})$, $\epsilon_{\vec{k}} = \epsilon_{M_1}(\vec{k})$, and $\epsilon_{M_i+\vec{q}-\vec{k}} = \epsilon_{M_1}(\vec{q}-\vec{k})$ [we also abbreviate $\epsilon_{M_1}(\vec{p})$ by $\epsilon^{M_1}_{\vec{p}}$]. We denote the external frequency by ip_0. For Matsubara sums, we use

$$T\sum_{i\omega} \frac{1}{(i\omega-\epsilon_1)(i\omega-\epsilon_2)} = \frac{n_F(\epsilon_1)-n_F(\epsilon_2)}{\epsilon_1-\epsilon_2}, \tag{C14}$$

$$T\sum_{i\omega} \frac{1}{(i\omega-\epsilon_1)(i\omega-\epsilon_2)(i\omega-\epsilon_3)} = \frac{n_F(\epsilon_1)}{(\epsilon_1-\epsilon_2)(\epsilon_1-\epsilon_3)} - \frac{n_F(\epsilon_2)}{(\epsilon_1-\epsilon_2)(\epsilon_2-\epsilon_3)} + \frac{n_F(\epsilon_3)}{(\epsilon_1-\epsilon_3)(\epsilon_2-\epsilon_3)}, \tag{C15}$$

$$T\sum_{i\omega} \frac{1}{(i\omega-\epsilon_1)^2(i\omega-\epsilon_2)} = \frac{n_F'(\epsilon_1)}{\epsilon_1-\epsilon_2} - \frac{n_F(\epsilon_1)}{(\epsilon_1-\epsilon_2)^2} + \frac{n_F(\epsilon_2)}{(\epsilon_1-\epsilon_2)^2}, \tag{C16}$$

and $n_F(ip_0+\epsilon) = -n_B(\epsilon)$, $n_B(\epsilon_2-\epsilon_1)[n_F(\epsilon_1)-n_F(\epsilon_2)] = n_F(-\epsilon_1)n_F(\epsilon_2)$, where n_F is the Fermi and n_B the Bose function. We obtain for the coupled particle-particle/particle-hole diagram

$$\begin{aligned}
&2T^2\sum_{k_0,q_0}\int d\vec{k}\int d\vec{q}\frac{1}{\left(iq_0-\epsilon^{M_1}_{\vec{q}}\right)^2\left(ik_0-\epsilon^{M_1}_{\vec{k}}\right)\left(-ik_0+iq_0+ip_0-\epsilon^{M_1}_{\vec{q}-\vec{k}}\right)}\\
&= 2\int d\vec{k}\int d\vec{q}\left\{\left[1-n_F\left(\epsilon^{M_1}_{\vec{q}-\vec{k}}\right)-n_F\left(\epsilon^{M_1}_{\vec{k}}\right)\right]\left[\frac{-n_F'\left(\epsilon^{M_1}_{\vec{q}}\right)}{\left(ip_0+\epsilon^{M_1}_{\vec{q}}-\epsilon^{M_1}_{\vec{k}}+\epsilon^{M_1}_{\vec{q}-\vec{k}}\right)}+\frac{n_F\left(\epsilon^{M_1}_{\vec{q}}\right)}{\left(ip_0+\epsilon^{M_1}_{\vec{q}}-\epsilon^{M_1}_{\vec{k}}+\epsilon^{M_1}_{\vec{q}-\vec{k}}\right)^2}\right]\right.\\
&\left.+\frac{n_F\left(\epsilon^{M_1}_{\vec{k}}\right)n_F\left(\epsilon^{M_1}_{\vec{k}-\vec{q}}\right)}{\left(ip_0+\epsilon^{M_1}_{\vec{q}}-\epsilon^{M_1}_{\vec{k}}+\epsilon^{M_1}_{\vec{q}-\vec{k}}\right)^2}\right\}.
\end{aligned} \tag{C17}$$

To see the temperature dependence of this expression, we rescale $k_x = T^{1/4}\tilde{k}_x$, $k_y = \sqrt{T}\tilde{k}_y$, $q_x = T^{1/4}\tilde{q}_x$, $q_y = \sqrt{T}\tilde{q}_y$ and express the external frequency as $p_0 = (2n+1)i\pi T$, which yields

$$\begin{aligned}
&\frac{2}{\sqrt{T}}\int d\vec{\tilde{k}}\int d\vec{\tilde{q}}\left\{\left[1-\tilde{n}_F\left(\epsilon^{M_1}_{\tilde{q}-\tilde{k}}\right)-n_F\left(\epsilon^{M_1}_{\tilde{k}}\right)\right]\left[\frac{[4\cosh^2\left(\epsilon^{M_1}_{\tilde{q}}\right)]^{-1}}{\left[(2n+1)i\pi+\epsilon^{M_1}_{\tilde{q}}-\epsilon^{M_1}_{\tilde{k}}+\epsilon^{M_1}_{\tilde{q}-\tilde{k}}\right]}+\frac{\tilde{n}_F\left(\epsilon^{M_1}_{\tilde{q}}\right)}{\left[(2n+1)i\pi+\epsilon^{M_1}_{\tilde{q}}-\epsilon^{M_1}_{\tilde{k}}+\epsilon^{M_1}_{\tilde{q}-\tilde{k}}\right]^2}\right]\right.\\
&\left.+\frac{\tilde{n}_F\left(\epsilon^{M_1}_{\tilde{k}}\right)\tilde{n}_F\left(\epsilon^{M_1}_{\tilde{k}-\tilde{q}}\right)}{\left[(2n+1)i\pi+\epsilon^{M_1}_{\tilde{q}}-\epsilon^{M_1}_{\tilde{k}}+\epsilon^{M_1}_{\tilde{q}-\tilde{k}}\right]^2}\right\}
\end{aligned} \tag{C18}$$

where we defined $\tilde{n}_F(x) = 1/[1+\exp(x)]$. The integrand is finite and independent of temperature, so indeed we obtain the correct temperature dependence $T^{2\kappa}$ for $\kappa = 1/4$. The same is true for the second integral in Eq. (C9). In the particle-hole channel, we get

$$\begin{aligned}
&-2T^2\sum_{k_0,q_0}\int d\vec{k}\int d\vec{q}\frac{1}{\left(iq_0-\epsilon^{M_1}_{\vec{q}}\right)^2\left(ik_0-\epsilon^{M_1}_{\vec{k}}\right)\left(ik_0-iq_0+ip_0-\epsilon^{M_1}_{\vec{k}-\vec{q}}\right)}\\
&= -2\int d\vec{k}\int d\vec{q}\left\{\left[n_F\left(\epsilon^{M_1}_{\vec{k}}\right)-n_F\left(\epsilon^{M_1}_{\vec{k}-\vec{q}}\right)\right]\left(\frac{n_F'\left(\epsilon^{M_1}_{\vec{q}}\right)}{ip_0+\epsilon^{M_1}_{\vec{q}}+\epsilon^{M_1}_{\vec{k}}-\epsilon^{M_1}_{\vec{k}-\vec{q}}}-\frac{n_F\left(\epsilon^{M_1}_{\vec{q}}\right)}{\left(ip_0+\epsilon^{M_1}_{\vec{q}}+\epsilon^{M_1}_{\vec{k}}-\epsilon^{M_1}_{\vec{k}-\vec{q}}\right)^2}\right)\right.\\
&\left.-n_F\left(\epsilon^{M_1}_{\vec{k}-\vec{q}}\right)\frac{1-2n_F\left(\epsilon^{M_1}_{\vec{k}}\right)}{\left(ip_0+\epsilon^{M_1}_{\vec{q}}+\epsilon^{M_1}_{\vec{k}}-\epsilon^{M_1}_{\vec{k}-\vec{q}}\right)^2}\right\},
\end{aligned} \tag{C19}$$

which after rescaling is also proportional to $1/\sqrt{T}$. We can calculate the remaining integrals numerically. The calculation does indeed show that there is a factor of order $\mathcal{O}(1)$ difference between the perturbation expansion and the RG. These results can be generalized to arbitrary loop order with the result that the iterative solution of the RG equations

reproduces the temperature dependence, which one obtained in the order-by-order diagrammatic expansion, and the prefactors are generally different because for power-law-singular DOS the momentum integrations do not factorize.

We note that the discrepancy between the perturbation expansion and the RG may be systematically studied by employing advanced truncation schemes such as, e.g., the recently developed multiloop functional RG [38].

APPENDIX D: THREE-PATCH RG FROM FUNCTIONAL RG

To investigate the quantum many-body instabilities of our model we employ a parquet RG approach. The parquet RG flow equations can be straightforwardly derived within a more general functional integral framework based on a one-loop exact FRG flow equation for the one-particle irreducible vertices of a correlated fermion system (see Refs. [39–41] for reviews).

With this renormalization-group scheme we can then identify the leading instabilities in the presence of competing interactions by successively integrating out fermion degrees of freedom starting from an initial RG scale Λ_0, e.g., corresponding to the bandwidth down to the infrared scale $\Lambda \to 0$. We now briefly set up the functional RG approach.

We consider the action for a many-fermion system corresponding to our model Hamiltonian, i.e.,

$$S[\bar{\psi}, \psi] = -\left(\bar{\psi}, G_0^{-1}\psi\right) + V[\bar{\psi}, \psi], \tag{D1}$$

where $\bar{\psi}$ and ψ are the Grassmann-valued fermion field degrees of freedom; the first term is the quadratic part including the free fermion propagator $G_0(\omega_n, \vec{k}, b) = 1/[i\omega_n - \epsilon_b(\vec{k})]$, the Matsubara frequency ω_n, and wave vector $\vec{k}$. The energy dispersion $\epsilon_b(\vec{k})$ with band index b follows from diagonalization of the free part of the Hamiltonian H_0 and we assume that the fermionic propagator is diagonal with respect to the spin quantum number. The second term $V[\bar{\psi}, \psi]$ in the above equation is the interaction term, which is quartic in the fermionic fields $\bar{\psi}$ and ψ and can be inferred from the interaction part of the Hamiltonian.

To set up the functional RG flow equations, the bare propagator is regularized by an infrared momentum cutoff represented by the scale Λ:

$$G_0(\omega_n, \vec{k}, b) \to G_0^{\Lambda}(\omega_n, \vec{k}, b). \tag{D2}$$

The purpose of the regularization and the introduction of the modified propagator G_0^{Λ} is to cut off infrared modes below the scale Λ and the implementation of this regularization can be realized in different ways, i.e., employing a momentum cutoff, a frequency cutoff, or a temperature cutoff. We leave this choice open for the moment, as it does not affect the structure of the FRG equations.

The modified propagator G_0^{Λ} is now used in the generating functional for the one-particle irreducible correlation functions and an exact flow equation is generated upon variation with respect to the cutoff scale Λ. More explicitly, we start with the generating functional for the fully connected correlation functions [42]:

$$\mathcal{G}[\bar{\eta}, \eta] = -\ln \int \mathcal{D}\psi \mathcal{D}\bar{\psi}\; e^{-S[\bar{\psi},\psi]+(\bar{\eta},\psi)+(\bar{\psi},\eta)}. \tag{D3}$$

For convenience, we consider the Legendre transform of $\mathcal{G}[\bar{\eta}, \eta]$, i.e., $\Gamma[\bar{\psi}, \psi] = (\bar{\eta}, \psi) + (\bar{\psi}, \eta) + \mathcal{G}[\bar{\eta}, \eta]$, which is called the effective action and which generates the one-particle irreducible correlation functions. Note that the field arguments in the effective action Γ are $\psi = -\partial\mathcal{G}/\partial\bar{\eta}$ and $\bar{\psi} = \partial\mathcal{G}/\partial\eta$.

Using the modified propagator G_0^{Λ} provides a cutoff dependence to the effective action $\Gamma \to \Gamma^{\Lambda}$. Taking the derivative of that scale-dependent effective action with respect to Λ produces an exact RG flow equation, reading

$$\frac{\partial}{\partial\Lambda}\Gamma^{\Lambda}[\bar{\psi}, \psi] = -\left(\bar{\psi}, \left(\dot{G}_0^{\Lambda}\right)^{-1}\psi\right) - \frac{1}{2}\mathrm{Tr}\left\{\left(\dot{\mathbf{G}}_0^{\Lambda}\right)^{-1}\left(\dot{\mathbf{\Gamma}}^{(2)\Lambda}[\bar{\psi}, \psi]\right)^{-1}\right\}, \tag{D4}$$

where $(\dot{\mathbf{G}}_0^{\Lambda})^{-1} = \mathrm{diag}((G_0^{\Lambda})^{-1}, (G_0^{\Lambda t})^{-1})$ and

$$\mathbf{\Gamma}^{(2)\Lambda}[\bar{\psi}, \psi] = \begin{pmatrix} \frac{\partial^2\Gamma^{\Lambda}}{\partial\bar{\psi}\partial\psi} & \frac{\partial^2\Gamma^{\Lambda}}{\partial\bar{\psi}\partial\bar{\psi}} \\ \frac{\partial^2\Gamma^{\Lambda}}{\partial\psi\partial\psi} & \frac{\partial^2\Gamma^{\Lambda}}{\partial\psi\partial\bar{\psi}} \end{pmatrix}. \tag{D5}$$

The initial condition of this differential equation is defined at the ultraviolet scale Λ_{UV} by the microscopic action $\Gamma^{\Lambda_{\mathrm{UV}}} = S$ and in the limit $\Lambda \to 0$ by the full quantum effective action Γ.

For tractability of the exact flow equation, we employ a truncation of the effective action Γ^{Λ} in the form of the vertex expansion ansatz:

$$\Gamma^{\Lambda}[\psi, \bar{\psi}] = \sum_{i=0}^{\infty}\frac{(-1)^i}{(i!)^2}\sum_{\substack{k_1,\ldots,k_i \\ k'_1,\ldots,k'_i}}\Gamma^{(2i)\Lambda}(k'_1,\ldots,k'_i,k_1,\ldots,k_i) \times \bar{\psi}(k'_1)\ldots\bar{\psi}(k'_i)\psi(k_i)\ldots\psi(k_1). \tag{D6}$$

This ansatz is inserted into the exact flow equation, which generates a hierarchy of flow equations for the one-particle irreducible vertex functions $\Gamma^{(2i)\Lambda}$. We truncate the tower of flow equations and exclusively consider the RG evolution of the two-particle interaction $\Gamma^{(4)\Lambda}$, which carries spin indices σ_i and multi-indices k collecting Matsubara frequencies, wave vectors, and band indices. We also neglect the self-energy feedback.

For the spin-rotation invariant system that we consider in this paper, the two-particle interaction can be written as

$$\Gamma^{(4)\Lambda}_{\sigma_1\sigma_2\sigma_3\sigma_4} = V^{\Lambda}\delta_{\sigma_1\sigma_3}\delta_{\sigma_2\sigma_4} - V^{\Lambda}\delta_{\sigma_1\sigma_4}\delta_{\sigma_2\sigma_3}, \tag{D7}$$

introducing the effective interaction vertex $V^{\Lambda} = V^{\Lambda}(k_1, k_2, k_3, b_4)$. For the analysis of instabilities, we are interested in the most singular part of V^{Λ}, which comes from the smallest Matsubara frequency, and we therefore only consider this one. Then, the RG flow of V^{Λ} can be derived from the exact flow equation Eq. (D4) and reads

$$\frac{d}{d\Lambda}V^{\Lambda} = \tau_{\mathrm{pp}} + \tau_{\mathrm{ph,d}} + \tau_{\mathrm{ph,cr}} \tag{D8}$$

with the particle-particle, the direct particle-hole, and the crossed particle-hole contributions on the right-hand side of the equation, reading

$$\tau_{\mathrm{pp}} = -\frac{1}{2}\sum\!\!\!\!\!\!\int V^{\Lambda}(k_1, k_2, k, b')L^{\Lambda}(k, q_{\mathrm{pp}})V^{\Lambda}(k, q_{\mathrm{pp}}, k_3, b_4),$$

where we defined $\sum\!\!\!\!\!\!\int = -A_{\mathrm{BZ}}^{-1} T \sum_{\omega} \int d^2k \sum_{b,b'}$ and A_{BZ} is the area of the Brillouin zone. Further, we have

$$\begin{aligned}\tau_{\mathrm{ph,d}} = \frac{1}{2} \sum\!\!\!\!\!\!\int [&2V^{\Lambda}(k_1, k, k_3, b') L^{\Lambda}(k, q_{\mathrm{d}}) V^{\Lambda}(q_{\mathrm{d}}, k_2, k, b_4) \\ &- V^{\Lambda}(k, k_1, k_3, b') L^{\Lambda}(k, q_{\mathrm{d}}) V^{\Lambda}(q_{\mathrm{d}}, k_2, k, b_4) \\ &- V^{\Lambda}(k, k_1, k_3, b') L^{\Lambda}(k, q_{\mathrm{d}}) V^{\Lambda}(k_2, q_{\mathrm{d}}, k, b_4)],\end{aligned}$$

and

$$\tau_{\mathrm{ph,cr}} = -\frac{1}{2} \sum\!\!\!\!\!\!\int V^{\Lambda}(k, k_2, k_3, b') L^{\Lambda}(k, q_{\mathrm{cr}}) V^{\Lambda}(k_1, q_{\mathrm{cr}}, k, b_4).$$

Above, we have used the definitions $q_{\mathrm{pp}} = -k + k_1 + k_2$, $q_{\mathrm{d}} = k + k_1 - k_3$, and $q_{\mathrm{cr}} = k + k_2 - k_3$ and the loop kernel

$$L^{\Lambda}(k, k') = \frac{d}{d\Lambda} \left[G_0^{\Lambda}(k) G_0^{\Lambda}(k') \right], \tag{D9}$$

with the free modified propagator G_0^{Λ} due to the neglect of the self-energy.

To derive the $N = 3$ patch parquet RG flow equations [see Eqs. (30)–(33)], we now introduce further approximations. Since we are interested in instabilities, we will consider only the strongest contributions to the flow of V^{Λ}, which come from wave vectors where the density of states is large, i.e., in our model the wave vectors at or near the $M_{1,2,3}$ points. Therefore, we introduce an $N = 3$ patch approximation by evaluating V^{Λ} only at the singularity momenta $M_{1,2,3}$. We exclusively take into account two-particle scattering processes on these three patches, as indicated in Fig. 4. Further, we assume that the interaction vertex is approximately constant within small patches surrounding the M_i points where the energy dispersion can be approximated by a pure saddle-point behavior. We can thus relate the interaction vertex V^{Λ} with the interaction couplings g_i (see Fig. 4):

$$V^{\Lambda}(M_i, M_j, M_i, M_j) = g_1, \quad i \neq j, \tag{D10}$$

$$V^{\Lambda}(M_i, M_j, M_j, M_i) = g_2, \quad i \neq j, \tag{D11}$$

$$V^{\Lambda}(M_i, M_i, M_j, M_j) = g_3, \quad i \neq j, \tag{D12}$$

$$V^{\Lambda}(M_i, M_i, M_i, M_i) = g_4. \tag{D13}$$

These relations can be put into the flow equation for the interaction vertex, Eq. (D8), yielding

$$\begin{aligned}
\frac{d}{d\Lambda} g_1 &= \frac{d}{d\Lambda} V^{\Lambda}(M_1, M_2, M_1, M_2) = \tau_{\mathrm{pp}}(M_1, M_2, M_1, M_2) + \tau_{\mathrm{ph,d}}(M_1, M_2, M_1, M_2) + \tau_{\mathrm{ph,cr}}(M_1, M_2, M_1, M_2), \\
\frac{d}{d\Lambda} g_2 &= \frac{d}{d\Lambda} V^{\Lambda}(M_1, M_2, M_2, M_1) = \tau_{\mathrm{pp}}(M_1, M_2, M_2, M_1) + \tau_{\mathrm{ph,d}}(M_1, M_2, M_2, M_1) + \tau_{\mathrm{ph,cr}}(M_1, M_2, M_2, M_1), \\
\frac{d}{d\Lambda} g_3 &= \frac{d}{d\Lambda} V^{\Lambda}(M_1, M_1, M_2, M_2) = \tau_{\mathrm{pp}}(M_1, M_1, M_2, M_2) + \tau_{\mathrm{ph,d}}(M_1, M_1, M_2, M_2) + \tau_{\mathrm{ph,cr}}(M_1, M_1, M_2, M_2), \\
\frac{d}{d\Lambda} g_4 &= \frac{d}{d\Lambda} V^{\Lambda}(M_1, M_1, M_1, M_1) = \tau_{\mathrm{pp}}(M_1, M_1, M_1, M_1) + \tau_{\mathrm{ph,d}}(M_1, M_1, M_1, M_1) + \tau_{\mathrm{ph,cr}}(M_1, M_1, M_1, M_1).
\end{aligned}$$

Evaluating the various channels' contributions within the small patches around the M points and for the respective wave-vector configurations then yields—after some straightforward algebra—the flow equations for the interaction couplings g_i, $i \in \{1, 2, 3, 4\}$ presented in the main text [see Eqs. (30)–(33)].

APPENDIX E: RG FIXED POINTS

We look for fixed points in the flow equations for the dimensionless couplings Eqs. (35)–(38), i.e., solutions $g^* = (g_1^*, g_2^*, g_3^*, g_4^*)$ of

$$\beta_{g_1} = \partial_t \hat{g}_1 = 0, \tag{E1}$$

$$\beta_{g_2} = \partial_t \hat{g}_2 = 0, \tag{E2}$$

$$\beta_{g_3} = \partial_t \hat{g}_3 = 0, \tag{E3}$$

$$\beta_{g_4} = \partial_t \hat{g}_4 = 0. \tag{E4}$$

In general, there are several fixed-point solutions and we are interested in their stability, i.e., if they are reachable without fine tuning. The stability of a fixed point can be determined by calculating the eigenvalues of the stability matrix evaluated at the fixed point:

$$\frac{\partial}{\partial_{g_i}} \beta_{g_j} \Big|_{g^*}. \tag{E5}$$

The fixed point is stable when all eigenvalues are negative. A negative eigenvalue corresponds to an irrelevant direction and a positive eigenvalue corresponds to a relevant one.

In general, the existence of a real solution and the number of relevant directions depend on d_0, N, and N_f. In our case, we set $N_f = 2$. We find that all fixed-point solutions possess one or more relevant directions, i.e., all are unstable. Among others, we can identify the interacting fixed point found in Ref. [17], where just one HOVH point was considered, so that only g_4 is present. In our more general setup with several HOVH points, it is given by

$$g_1^* = g_2^* = g_3^* = 0 \quad \text{and} \quad g_4^* = \frac{1}{1 - d_0} \kappa. \tag{E6}$$

It has two relevant directions for $d_0 < 1/3$ and one relevant direction for $d_0 > 1/3$. Furthermore, there are two more possible solutions with just one relevant direction for sufficiently small d_0.

For $N = 2$ and $d_0 \geqslant 2(N-1)/[N^2 + 2(N-1)]$, they are

$$g_1^* = g_3^* = 0,$$

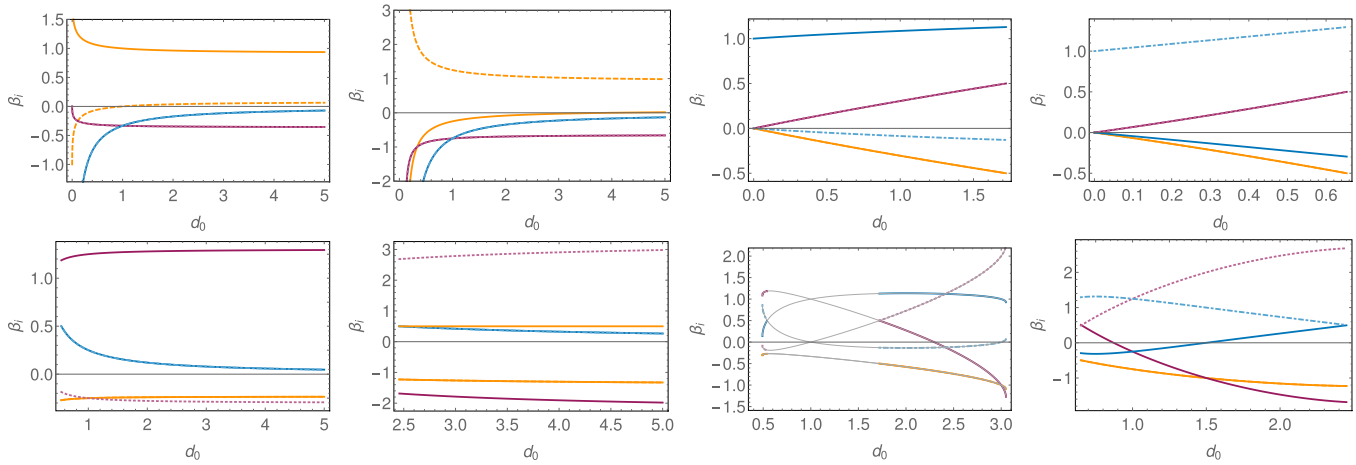

FIG. 13. Susceptibility exponents for the stable fixed trajectories as a function of d_0. They correspond to I–VIII from left to right, from top to bottom. s-wave spin, solid orange; d-wave spin, dashed light orange; s-wave charge, solid purple; d-wave charge, dotted light purple; s-wave SC, solid blue; d-wave SC, dot-dashed light blue. Fixed trajectory VII has two regimes of stability; for clarity we connect the exponents in both regimes by thin lines.

$$g_2^* = \frac{(N-2)(1-2d_0)}{2d_0\{(N-2)^2 - d_0[N^2-6(N-1)]\}}\kappa \mp \frac{\sqrt{d_0\{d_0[N^2+2(N-1)]-2(N-1)\}}}{2d_0\{(N-2)^2 - d_0[N^2-6(N-1)]\}}\kappa,$$

$$g_4^* = \frac{d_0[2+N(N-2)]}{2d_0\{(N-2)^2 - d_0[N^2-6(N-1)]\}}\kappa \pm \frac{(N-2)\sqrt{d_0\{d_0[N^2+2(N-1)]-2(N-1)\}}}{2d_0\{(N-2)^2 - d_0[N^2-6(N-1)]\}}\kappa.$$

For $N = 3$, they have two relevant directions. The two solutions with one relevant direction for $N = 3$ are

$$g_1^* = \frac{9+16d_0-\sqrt{d_0\left(72+481d_0+72d_0^2\right)}}{9d_0(d_0-1)}\kappa,$$

$$g_2^* = -2g_4^* = \frac{25d_0-\sqrt{d_0\left(72+481d_0+72d_0^2\right)}}{9d_0(d_0-1)}\kappa,$$

$$g_3^* = \frac{16d_0+9d_0^2-\sqrt{d_0\left(72+481d_0+72d_0^2\right)}}{9d_0(d_0-1)}\kappa, \quad \text{(E7)}$$

and for $d_0 < 9/13$

$$g_1^* = g_2^* = \frac{9+8d_0+\sqrt{d_0\left(108+213d_0+104d_0^2\right)}}{d_0(13d_0-9)}\kappa,$$

$$g_3^* = \frac{12d_0+13d_0^2+\sqrt{d_0\left(108+213d_0+104d_0^2\right)}}{d_0(13d_0-9)}\kappa,$$

$$g_4^* = -\frac{21d_0+\sqrt{d_0\left(108+213d_0+104d_0^2\right)}}{2d_0(13d_0-9)}\kappa. \quad \text{(E8)}$$

APPENDIX F: SUSCEPTIBILITY EXPONENTS

To determine the leading ordering tendency, we compare the susceptibilities for superconducting, charge, and spin orders. The largest susceptibility has the largest exponent [see Eqs. (47)–(51)]. Furthermore, the exponent has to be larger than 1/2 for the susceptibility to diverge approaching the critical scale. Based on the largest exponent, we assign the ordering tendency to the fixed trajectories. We plot the different exponents as a function of d_0 for the stable fixed trajectories in Fig. 13.

[1] L. Van Hove, The occurrence of singularities in the elastic frequency distribution of a crystal, Phys. Rev. **89**, 1189 (1953).

[2] K. L. Hur and T. M. Rice, Superconductivity close to the Mott state: From condensed-matter systems to superfluidity in optical lattices, Ann. Phys. (NY) **324**, 1452 (2009).

[3] R. Nandkishore, L. Levitov, and A. Chubukov, Chiral superconductivity from repulsive interactions in doped graphene, Nat. Phys. **8**, 158 (2012).

[4] M. L. Kiesel, C. Platt, W. Hanke, D. A. Abanin, and R. Thomale, Competing many-body instabilities and unconventional superconductivity in graphene, Phys. Rev. B **86**, 020507(R) (2012).

[5] W.-S. Wang, Y.-Y. Xiang, Q.-H. Wang, F. Wang, F. Yang, and D.-H. Lee, Functional renormalization group and variational Monte Carlo studies of the electronic instabilities in graphene near $\frac{1}{4}$ doping, Phys. Rev. B **85**, 035414 (2012).

[6] R. Nandkishore, R. Thomale, and A. V. Chubukov, Superconductivity from weak repulsion in hexagonal lattice systems, Phys. Rev. B **89**, 144501 (2014).

[7] A. M. Black-Schaffer and C. Honerkamp, Chiral d-wave superconductivity in doped graphene, J. Phys.: Condens. Matter **26**, 423201 (2014).

[8] R. Nandkishore, G.-W. Chern, and A. V. Chubukov, Itinerant Half-Metal Spin-Density-Wave State on the Hexagonal Lattice, Phys. Rev. Lett. **108**, 227204 (2012).

[9] G.-W. Chern, R. M. Fernandes, R. Nandkishore, and A. V. Chubukov, Broken translational symmetry in an emergent paramagnetic phase of graphene, Phys. Rev. B **86**, 115443 (2012).

[10] S. Link, S. Forti, A. Stöhr, K. Küster, M. Rösner, D. Hirschmeier, C. Chen, J. Avila, M. C. Asensio, A. A. Zakharov, T. O. Wehling, A. I. Lichtenstein, M. I. Katsnelson, and U. Starke, Introducing strong correlation effects into graphene by gadolinium intercalation, Phys. Rev. B **100**, 121407(R) (2019).

[11] J. L. McChesney, A. Bostwick, T. Ohta, T. Seyller, K. Horn, J. González, and E. Rotenberg, Extended Van Hove Singularity and Superconducting Instability in Doped Graphene, Phys. Rev. Lett. **104**, 136803 (2010).

[12] N. F. Yuan, H. Isobe, and L. Fu, Magic of high-order Van Hove singularity, Nat. Commun. **10**, 1 (2019).

[13] D. Di Sante, X. Wu, M. Fink, W. Hanke, and R. Thomale, Triplet superconductivity in the Dirac semimetal germanene on a substrate, Phys. Rev. B **99**, 201106(R) (2019).

[14] A. Shtyk, G. Goldstein, and C. Chamon, Electrons at the monkey saddle: A multicritical Lifshitz point, Phys. Rev. B **95**, 035137 (2017).

[15] D. V. Efremov, A. Shtyk, A. W. Rost, C. Chamon, A. P. Mackenzie, and J. J. Betouras, Multicritical Fermi Surface Topological Transitions, Phys. Rev. Lett. **123**, 207202 (2019).

[16] A. Ramires, P. Coleman, A. H. Nevidomskyy, and A. M. Tsvelik, $\beta-YbAlB_4$: A Critical Nodal Metal, Phys. Rev. Lett. **109**, 176404 (2012).

[17] H. Isobe and L. Fu, Supermetal, Phys. Rev. Res. **1**, 033206 (2019).

[18] N. F. Q. Yuan and L. Fu, Classification of critical points in energy bands based on topology, scaling, and symmetry, Phys. Rev. B **101**, 125120 (2020).

[19] A. Chandrasekaran, A. Shtyk, J. J. Betouras, and C. Chamon, Catastrophe theory classification of fermi surface topological transitions in two dimensions, Phys. Rev. Res. **2**, 013355 (2020).

[20] N. Furukawa, T. M. Rice, and M. Salmhofer, Truncation of a Two-Dimensional Fermi Surface due to Quasiparticle Gap Formation at the Saddle Points, Phys. Rev. Lett. **81**, 3195 (1998).

[21] C. Honerkamp and M. Salmhofer, Temperature-flow renormalization group and the competition between superconductivity and ferromagnetism, Phys. Rev. B **64**, 184516 (2001).

[22] C. Husemann and M. Salmhofer, Efficient parametrization of the vertex function, Ω scheme, and the t, t' Hubbard model at van Hove filling, Phys. Rev. B **79**, 195125 (2009).

[23] Y.-P. Lin and R. M. Nandkishore, Chiral twist on the high-T_c phase diagram in Moiré heterostructures, Phys. Rev. B **100**, 085136 (2019).

[24] S. Maiti and A. V. Chubukov, Superconductivity from repulsive interaction, in *Lectures on the Physics of Strongly Correlated Systems XVII: Seventeenth Training Course in the Physics of Strongly Correlated Systems*, edited by A. Avella and F. Mancini, AIP Conf. Proc. No. 1550 (AIP, New York, 2013), p. 3.

[25] W. Metzner, C. Castellani, and C. D. Castro, Fermi systems with strong forward scattering, Adv. Phys. **47**, 317 (1998).

[26] J. M. Murray and O. Vafek, Renormalization group study of interaction-driven quantum anomalous hall and quantum spin hall phases in quadratic band crossing systems, Phys. Rev. B **89**, 201110(R) (2014).

[27] A. V. Chubukov, M. Khodas, and R. M. Fernandes, Magnetism, Superconductivity, and Spontaneous Orbital Order in Iron-Based Superconductors: Which Comes First and Why? Phys. Rev. X **6**, 041045 (2016).

[28] L. Classen, R.-Q. Xing, M. Khodas, and A. V. Chubukov, Interplay Between Magnetism, Superconductivity, and Orbital Order in 5-Pocket Model for Iron-Based Superconductors: Parquet Renormalization Group Study, Phys. Rev. Lett. **118**, 037001 (2017).

[29] R.-Q. Xing, L. Classen, M. Khodas, and A. V. Chubukov, Competing instabilities, orbital ordering, and splitting of band degeneracies from a parquet renormalization group analysis of a four-pocket model for iron-based superconductors: Application to FeSe, Phys. Rev. B **95**, 085108 (2017).

[30] M. L. Kiesel, C. Platt, and R. Thomale, Unconventional Fermi Surface Instabilities in the Kagome Hubbard Model, Phys. Rev. Lett. **110**, 126405 (2013).

[31] M. Hecker and J. Schmalian, Vestigial nematic order and superconductivity in the doped topological insulator $Cu_xBi_2Se_3$, npj Quantum Mater. **3**, 26 (2018).

[32] A. Little, C. Lee, C. John, S. Doyle, E. Maniv, N. L. Nair, W. Chen, D. Rees, J. W. F. Venderbos, R. M. Fernandes *et al.*, Observation of three-state nematicity in the triangular lattice antiferromagnet $Fe_{1/3}NbS_2$, Nat. Mater. **19**, 1062 (2020).

[33] S. Jin, W. Zhang, X. Guo, X. Chen, X. Zhou, and X. Li, Dynamical emergence of a Potts-nematic superfluid in a hexagonal sp^2 optical lattice, arXiv:1910.11880.

[34] J. W. F. Venderbos and R. M. Fernandes, Correlations and electronic order in a two-orbital honeycomb lattice model for twisted bilayer graphene, Phys. Rev. B **98**, 245103 (2018).

[35] R. M. Fernandes and J. W. F. Venderbos, Nematicity with a twist: Rotational symmetry breaking in a Moiré superlattice, Sci. Adv. **6**, eaba8834 (2020).

[36] L. Classen, C. Honerkamp, and M. M. Scherer, Competing phases of interacting electrons on triangular lattices in Moiré heterostructures, Phys. Rev. B **99**, 195120 (2019).

[37] Y.-P. Lin and R. M. Nandkishore, Kohn-Luttinger superconductivity on two orbital honeycomb lattice, Phys. Rev. B **98**, 214521 (2018).

[38] F. B. Kugler and J. von Delft, Multiloop Functional Renormalization Group That Sums Up All Parquet Diagrams, Phys. Rev. Lett. **120**, 057403 (2018).

[39] W. Metzner, M. Salmhofer, C. Honerkamp, V. Meden, and K. Schönhammer, Functional renormalization group approach to correlated fermion systems, Rev. Mod. Phys. **84**, 299 (2012).

[40] C. Platt, W. Hanke, and R. Thomale, Functional renormalization group for multi-orbital Fermi surface instabilities, Adv. Phys. **62**, 453 (2013).

[41] N. Dupuis, L. Canet, A. Eichhorn, W. Metzner, J. M. Pawlowski, M. Tissier, and N. Wschebor, The nonperturbative functional renormalization group and its applications, arXiv:2006.04853.

[42] J. W. Negele, *Quantum Many-Particle Systems* (CRC, Boca Raton, FL, 2018).